

A Novel Image Denoising Algorithm Using Concepts of Quantum Many-Body Theory

Sayantan Dutta^{1,2,*}, Adrian Basarab³, Bertrand Georgeot², and Denis Kouamé¹

¹Institut de Recherche en Informatique de Toulouse, UMR CNRS 5505, Université de Toulouse, France

²Laboratoire de Physique Théorique, Université de Toulouse, CNRS, UPS, France

³ Université de Lyon, INSA-Lyon, Université Claude Bernard Lyon 1, UJM-Saint Etienne, CNRS, Inserm, CREATIS UMR 5220, U1206, Villeurbanne, France

Abstract

Sparse representation of real-life images is a very effective approach in imaging applications, such as denoising. In recent years, with the growth of computing power, data-driven strategies exploiting the redundancy within patches extracted from one or several images to increase sparsity have become more prominent. This paper presents a novel image denoising algorithm exploiting such an image-dependent basis inspired by the quantum many-body theory. Based on patch analysis, the similarity measures in a local image neighborhood are formalized through a term akin to interaction in quantum mechanics that can efficiently preserve the local structures of real images. The versatile nature of this adaptive basis extends the scope of its application to image-independent or image-dependent noise scenarios without any adjustment. We carry out a rigorous comparison with contemporary methods to demonstrate the denoising capability of the proposed algorithm regardless of the image characteristics, noise statistics and intensity. We illustrate the properties of the hyperparameters and their respective effects on the denoising performance, together with automated rules of selecting their values close to the optimal one in experimental setups with ground truth not available. Finally, we show the ability of our approach to deal with practical images denoising problems such as medical ultrasound image despeckling applications.

Index Terms

Quantum many-body interaction, Adaptive denoiser, Quantum denoiser, Quantum image processing, Adaptive transformation.

I. INTRODUCTION

Over time, original methods from various branches of science have enriched the literature on digital image processing, and specifically the fundamental question of signal or image denoising, such as statistics [1], probability theory [2], [3], graph theory [4]–[6] or differential equations [7], [8]. For the particular case of image restoration addressed herein, number of methods are based on sparse representations into a given basis, with most of the true image described by the projections on a few basis vectors. This enables to efficiently store and restore the image. Such sparse representations [9], [10] depend on both the transformation chosen and the nature of the image. Traditionally, all these methods exploit few explicit or underlying hypotheses about the image to restore, for example, piece-wise smoothness, but are not strong enough to capture the complex textures present in the true image.

With the growth of computing power, data-driven strategies to increase the sparsity and overcome the limitations of general transforms have become more prominent in recent decades. One such approach is to learn overcomplete dictionaries from training image sets [11], [12]. Another method is based on patch-based schemes, using patch neighborhood as a feature vector. For example, block-matching and 3D filtering known as BM3D creates 3D data arrays by grouping similar image fragments before computing a sparse representation applying 3D transformations [13], [14].

The non-local means (NLM) algorithm brought a different perspective to the image denoising problem, where each estimated image pixel intensity is a weighted average of pixels centered at patches that are similar to the patch centered at the estimated pixel [15]. An alternative patch-based NLM approach projects image patches into a lower dimensional subspace using principal component analysis (PCA) before performing the weighted average for denoising [16], [17]. Later on, various schemes were proposed in the literature to accelerate or to improve the NLM performance, such as a fast NLM algorithm with a probabilistic early termination [18], quadtree-based NLM with locally adaptive PCA [19], fast processing using statistical nearest neighbors strategy [20], adaptive neighborhoods [21], patch-based locally optimal Wiener filtering [22] and others [23]–[30]. These NLM-based schemes are known as a powerful way of denoising exploiting similar patches from the whole image. Hence, the patch neighborhood gives an effective way of preserving the local structures of an image where neighborhood similarity is the key ingredient.

* Corresponding author: Sayantan Dutta (sayantan.dutta@irit.fr; sayantan.dutta110@gmail.com)

This paper explores such an approach of exploiting the image neighborhood by borrowing tools from quantum mechanics, precisely, the quantum interactions. Quantum theory is the underlying theory of nature, which governs our world at a fundamental level, and classical mechanics is merely a limiting behavior of quantum mechanics. In classical theory, the position and momentum of a particle are determined precisely, whereas in quantum theory they are given by a probability distribution encoded in the wave function. The wave function in turn can be computed as solution of a wave equation known as the Schrödinger equation. Over the past few years, new proposals to use such wave functions as a basis in imaging applications, such as image feature extraction [31]–[33], denoising [34], [35], deconvolution [36], [37] or others [38], [39] have been proposed in the literature. However, all the existing approaches have been built on the theory of single-particle quantum systems.

In this paper, we propose a novel image representation algorithm well adapted for denoising based on the theory of quantum many-body interaction. In the case of a system containing two or more quantum particles, they can influence each other's quantum state through quantum interactions. The main idea of this work is to adapt ideas from this theory to extend the concept of interaction to imaging problems. More precisely, the proposed framework consists in quantum interactions between image patches where interactions reflect patch similarity measures in a local neighborhood. In this way, each patch acts as a single-particle system, and the whole collection, that is the entire image, behaves as a many-body system where interactions describe regional similarities to neighboring patches. Preliminary results on Gaussian denoising were presented in [40]. Herein, we show that this method constitutes a robust generalized formalism for image-independent and image-dependent noise models. The extension of [40] primarily lies in: (i) the characterization of the hyperparameters and automated ways to predict their optimal values with limited knowledge about the input image, (ii) investigation on the denoising possibilities beyond Gaussian statistics without any modification of the algorithms, (iii) a detailed discussion of denoising performance compared to state-of-the-art methods for both image-independent and image-dependent scenarios, (iv) application on real medical data for ultrasound image despeckling.

Earlier proposed single-particle based schemes [31]–[37] have proven their good restoration abilities for different noise models, but are too simple to take advantage of the structural properties of the image and are computationally costly at large scale. As we will show, the proposed generalized framework based on the use of quantum many-body physics improves the previous methods on both counts, building a more versatile computationally efficient adaptive basis that considers similarities between neighboring image patches.

In general, it may seem that there is a close architectural resemblance between the NLM and the proposed many-body scheme since similarity measure is the key for both cases. However, the two methods are different from several perspectives. The NLM image denoising algorithm exploits the self-similarities among the image patches to obtain the similarity weights resulting into a non-local weighted average scheme for denoising. The proposed approach brings non-local characteristics within the quantum framework, where interactions between neighboring patches preserve the local structural similarities. For each patch, these interactions convey the structural information into a quantum adaptive basis offering a good sparsifying transformation at a patch level further used for denoising. It turns out that such a theory can be elegantly written using multi-particle quantum theory instead of the single-particle one.

In the paper, we first present briefly the previously proposed decomposition concept using a quantum adaptive basis [35] based on single-particle theory with its limitations in Section II-A, and then introduce its generalization using many-body quantum theory for imaging problems in Section II-B. Our image denoising algorithm is described in detail in Section III. We then turn to numerical implementation of the method on several examples in Section IV. We first explore ways to propose automated rules for hyperparameters selection, and then display numerical results showing that the ability of the proposed method in reducing low and high intensity noise regardless of the noise statistics. We also show its good performance in real-life medical ultrasound (US) image despeckling applications. Finally we end with conclusions and future perspectives in Section V.

II. QUANTUM MANY-BODY THEORY FOR IMAGING

A. Quantum theory for a single-particle system

1) *Quantum theory:* Before detailing the proposed method, we briefly review, for self consistency, the quantum mechanical method for denoising built on single-particle theory introduced in [35]. For more details on quantum theory, one may refer to one of the many textbooks on this subject, e.g. [41]–[43].

In a non-relativistic single-particle quantum system the wave function $\psi(z)$ describes a particle with energy E in a potential $V(z)$ and satisfies the stationary Schrödinger equation:

$$-\frac{\hbar^2}{2m}\nabla^2\psi(z) + V(z)\psi(z) = E\psi(z), \quad (1)$$

with m , \hbar , ∇ , and z are respectively the mass of the quantum particle, the Planck constant, the gradient operator, and the spatial coordinate. The wave function $\psi(z)$ is an element of the Hilbert space of L^2 -integrable functions, and its modulus square *i.e.*, $|\psi(z)|^2$, gives the probability of presence of the particle at some point z on the potential $V(z)$.

The wave function solutions of (1) form a complete set of basis vectors of the Hilbert space with the following properties: i) Wave vectors are oscillating functions. ii) Oscillation frequency increases with increasing energy E . iii) The basis vectors

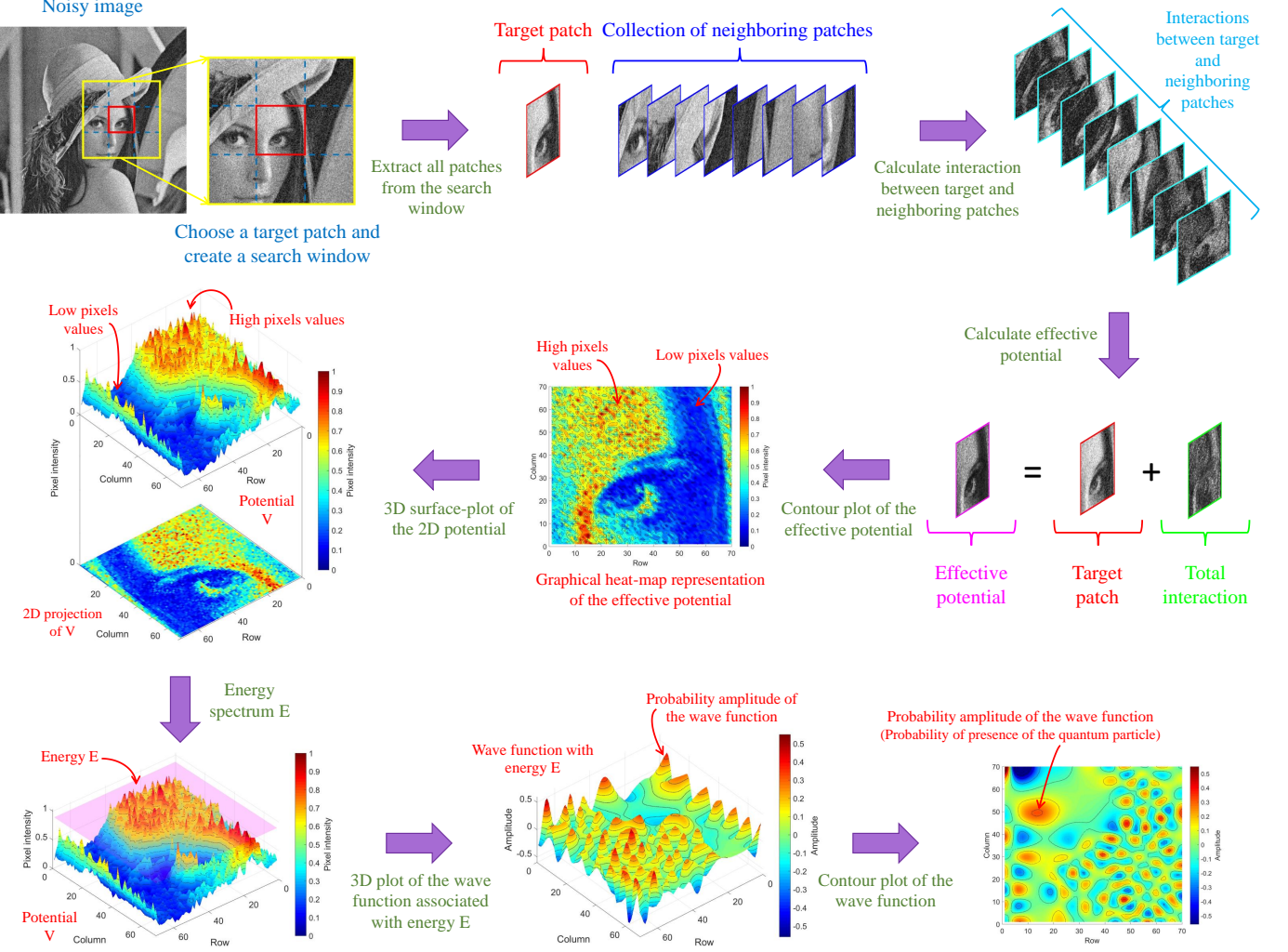


Fig. 1. A simple example of the construction of adaptive vectors from many-patch interaction.

oscillate with a local frequency proportional to $\sqrt{E - V(z)}$, thus for the same wave function the frequency differs locally depending on the local value of $E - V(z)$. iv) The hyperparameter $\hbar^2/2m$ controls the dependence of the local frequency on $E - V(z)$. These properties of the basis vectors are the key features to use them as an adaptive basis for an imaging problem. For a more detailed illustration of these features, we refer readers to [35].

2) *Application to imaging problems:* To adapt these concepts to image processing applications, the wave equation (1) is rewritten in operator notation leading to $\mathbf{H}\psi(z) = E\psi(z)$ with Hamiltonian operator $\mathbf{H} = -(\hbar^2/2m)\nabla^2 + \mathbf{V}(z)$. The eigenvectors of the Hamiltonian operator are the stationary solutions of (1).

For imaging applications, the space is finite and discretized, and the potential \mathbf{V} of the system may be defined as the image pixel values \mathbf{x} . This leads to a discretized problem, where the Hamiltonian operator becomes a finite matrix and can be used as a tool for constructing an adaptive basis [35]. This discretized Hamiltonian operator reads:

$$\mathbf{H}[i, j] = \begin{cases} \mathbf{x}[i] + 4\frac{\hbar^2}{2m} & \text{for } i = j, \\ -\frac{\hbar^2}{2m} & \text{for } i = j \pm 1, \\ -\frac{\hbar^2}{2m} & \text{for } i = j \pm n, \\ 0 & \text{otherwise,} \end{cases} \quad (2)$$

where $\mathbf{x} \in \mathbb{R}^{n^2}$ is an image (*i.e.*, $\mathbf{V} = \mathbf{x}$), and $\mathbf{x}[i]$ and $\mathbf{H}[i, j]$ represent respectively the i -th component of the image \mathbf{x} , vectorized in lexicographical order and the (i, j) -th component of the operator. Note that standard zero padding is used to handle the boundary conditions. A more detailed description of the Hamiltonian construction can be found in [35], [36]. The corresponding set of eigenvectors of the Hamiltonian operator (2) serves as the quantum adaptive basis on which the image is decomposed before denoising is performed by thresholding the coefficients in energy.

3) *Shortcomings of the single-particle theory in image processing:* This method of constructing an adaptive basis using quantum principles in a single-particle setting has already been studied in some of our previous works, notably for image denoising [35] and deconvolution [36], [37]. This adaptive method not only is effective for handling different noise statistics (e.g., Gaussian, Poisson) but also equally efficient for different levels of noise (low as well as high-intensity noise). Nevertheless, there are some technical and intrinsic challenges, such as:

- i) Structural features are crucial for imaging applications, but this adaptive approach does not take advantage of them.
- ii) The random noise present in the system leads to the well-known phenomenon of quantum localization [44] of the wave vectors. The presence of this subtle quantum phenomenon gives additional structures to the adaptive basis and makes it less effective for image denoising. This problem was cured in [35] by adding an additional step of low-pass filtering, for example, through a Gaussian filter with appropriate standard deviation, of the noisy image. This complicates the method and in particular entails the integration of a new hyperparameter (standard deviation) in the algorithm, which increases the complexity of hyperparameter tuning.
- iii) The computational burden of such a method can be quite large compared to other sophisticated state-of-the-art methods, thus preventing it from implementation in large-scale images.

In the following, we will show that these drawbacks can be addressed by constructing a new adaptive basis by exploiting quantum many-body theory, more precisely the physics of quantum interactions.

B. Quantum many-body theory for image processing

1) *Quantum theory for many particles:* The quantum theory described above is modified for a system with more than one particle. In particular, particle-to-particle interactions take place inside the quantum system. For a system with w particles the Hamiltonian operator for the many-body system becomes [45]:

$$H = - \sum_{a=1}^w \frac{\hbar^2}{2m_a} \nabla^2 + \frac{1}{2} \sum_{a=1}^w \sum_{b=1, b \neq a}^w V_{ab}, \quad (3)$$

where m_a is the mass of the a -th particle and the potential V_{ab} is a function of z_1, z_2, \dots, z_w , the spatial coordinates of the w particles. Thus, for a given energy E the associated wave function ψ depends on z_1, z_2, \dots, z_w , and satisfies a new Schrödinger equation:

$$H\psi(z_1, z_2, \dots, z_w) = E\psi(z_1, z_2, \dots, z_w). \quad (4)$$

2) *Application to image processing:* We propose to extend this multi-body theory to build an adaptive basis for imaging applications by assimilating similarities between patches into the quantum framework. Similar to non-local mean filter-based approaches, the proposed algorithm splits the image or a local region into small patches ranging from 1 to w . Each of these patches acts as a single-particle quantum system, which allows the Hamiltonian operator to be defined for each patch as follows:

$$\mathbf{H}_a = \underbrace{-\frac{\hbar^2}{2m_a} \nabla^2}_{\mathbf{H}_{0a}} + \underbrace{\mathbf{V}(z_a)}_{\mathbf{V}_a^{effective}} + \underbrace{\sum_{b=1, b \neq a}^w \mathbf{I}_{ab}}_{\mathbf{H}_{Ia}}, \quad a = 1, \dots, w, \quad (5)$$

where, \mathbf{H}_{0a} is the Hamiltonian in the patch A for a single particle system (as discretized in (2)). \mathbf{I}_{ab} and \mathbf{H}_{Ia} represent respectively the interaction between the A and B patches and the total interaction between the patch A and the other patches in the system. Thus, inside the patch A the effective potential $\mathbf{V}_a^{effective}$ is

$$\mathbf{V}_a^{effective} = \mathbf{V}(z_a) + \sum_{b=1, b \neq a}^w \mathbf{I}_{ab} = \mathbf{V}(z_a) + \mathbf{H}_{Ia}. \quad (6)$$

Therefore, we have a different adaptive basis for each patch containing a unique effective potential $\mathbf{V}_a^{effective}$ associated with an energy E_a . Fig. 1 depicts one such simple example of constructing adaptive vectors from the many-patch interaction concept. Thus the problem of finding the adaptive basis is transformed into the solution of the system of w equations, as follows:

$$\mathbf{H}_a \psi(z_a) = E_a \psi(z_a), \quad a = 1, 2, \dots, w. \quad (7)$$

where similar discretization procedures should be used in each patch as in (2).

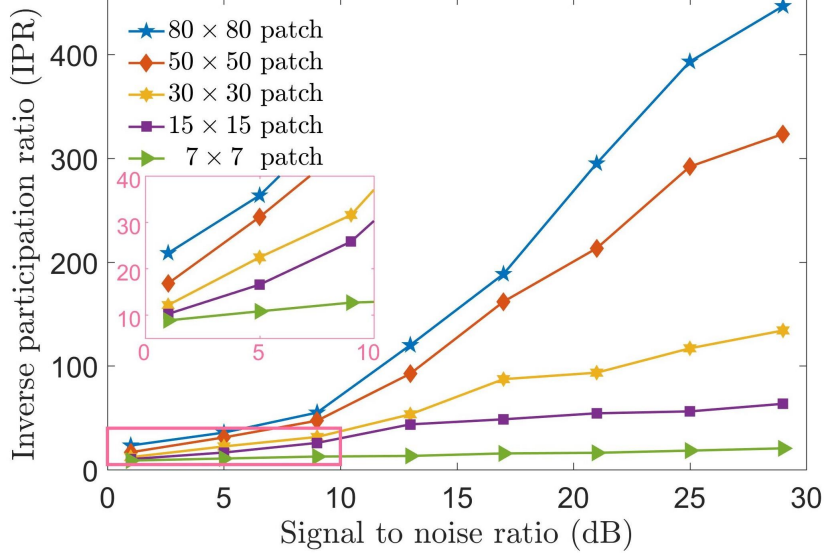


Fig. 2. Average inverse participation ratio (IPR) of all the adaptive basis vectors as a function of signal to noise ratio for the *Lena* image degraded by AWGN using different sizes of the image patch.

3) *Definition of the quantum interaction between two image patches:* Interaction between two or more objects is a universal phenomenon that governs the world at a very basic level, fundamentally classified into four groups: gravitational, electromagnetic, strong, and weak interactions. The gravitational and electromagnetic interactions have long-range properties characterized by power laws. We extend this concept to an imaging problem by introducing the interaction between two image patches, as follows:

- There is an inverse proportionality between the interaction and the square of the Euclidean distance (*i.e.*, physical distance) between the patches, *i.e.*, $\mathbf{I}_{ab} \propto \frac{1}{D_{ab}^2}$, where D_{ab} is the Euclidean distance between two patches denoted by \mathbf{A} and \mathbf{B} .
- There is a linear proportionality between the interaction and the absolute value of the pixel-wise difference between the patches. This process is defined pixel-wise, *i.e.*, $\mathbf{I}_{ab}^i \propto |\mathbf{A}^i - \mathbf{B}^i|$, $i = 1, 2, \dots, P_{dim}$, where superscript i and P_{dim} are associated with the i -th pixel and the number of pixels in every image patch respectively.

Hence, within the proposed image processing framework, the power law for an interacting many-patch system can be defined as

$$\mathbf{I}_{ab}^i = p \frac{|\mathbf{A}^i - \mathbf{B}^i|}{D_{ab}^2}, \quad i = 1, 2, \dots, P_{dim}, \quad (8)$$

where the proportionality constant p acts as a hyperparameter for the proposed formalism.

4) *Interaction and patch similarity in image processing:* In our many-patch model the proposed mathematical formalism of the power law interaction can be interpreted in the following way: i) two patches with similar pixel values have smaller interaction than the ones with very different values, ii) patches located far from each other have small interaction regardless of their pixel values. In other words, neighboring patches show high interactions if they are very different from each other based on pixel values, while distant patches are always less interactive despite their possible dissimilarity. Based on these principles, the power law manifests itself in such a way that the effective potential of the patch \mathbf{A} is $V_a^{effective}$. This is obtained after the combination of the initial potential (*i.e.*, the target patch itself) with the total interaction between the target patch and its neighboring patches, exploiting the concept of patch similarity in the local neighborhood. This local-similarity is a fundamental building block of real images that preserves structural features [15]. We note that power laws other than the inverse square law could be used, thus modifying the importance of distant patches compared to the nearby ones in the proposed methodology.

5) *Why the many-patch theory avoids the quantum localization problem:* The presence of random fluctuations in the potential of a quantum system leads to the phenomenon of quantum localization, also known as Anderson localization [44]. This is a property of wave functions in a disordered potential which makes them exponentially localized due to destructive interference. As a consequence, the adaptive basis vectors for various imaging problems are localized at different positions of the potential in presence of random noise, which makes the adaptive basis less suitable for image decomposition tasks. In [35], this challenge was solved by adding a cumbersome first step of image low-pass filtering, with an additional hyperparameter involved. A more detailed discussion of this phenomenon, in particular for image decomposition and denoising, can be found in our previous work [35].

In the framework of the many-patch theory described above, the decomposition is done at the level of the individual patch, much smaller than the full image. The inverse participation ratio (IPR) of the wave functions, defined as $1/\sum_i |\psi(i)|^4$ for a

wave function ψ , gives a measure of the localization. For a vector uniformly spread over L indices and zero elsewhere, the IPR is exactly L . More generally, the localization length of localized wave functions is proportional to the IPR. It is known from localization theory that this localization length decreases with the intensity of the disorder. Thus unless the noise is extremely strong, the localization length may be larger than the patch size, making the localization irrelevant for our problem. Fig. 2 shows the average IPR (measuring the localization length) of all the adaptive basis vectors for the *Lena* image degraded by additive white Gaussian noise (AWGN) with increasing signal to noise ratio (SNR) using different patch sizes. This illustration confirms that the IPR decreases with the SNR, but this effect reduces with patch size. For example, for a 80×80 patch, the IPR decreases rapidly with decreasing SNR (increasing noise intensity) and becomes less than the patch size for $\text{SNR} \leq 12$ dB, making the system extremely localized. However, for smaller patches like 7×7 , almost no such effect is visible for similar noise intensities. In other words, the localization effect becomes negligible in a small patch than in a large one and turns out to be irrelevant beyond a certain level of patch size. We found out that even for fairly strong noise it is always possible to find a patch size smaller than the average IPR that makes irrelevant the localization effect, avoiding the need of the low-pass filtering to create the adaptive basis.

III. QUANTUM MANY-PATCH INTERACTION FOR IMAGING APPLICATIONS: THE PROBLEM OF IMAGE DECOMPOSITION

A. Key principles of the proposed many-patch model

The objective of this work is to propose a methodology of an explicit construction of an adaptive basis related to the many-body interaction theory under the principles recalled here [40]:

- Every small patch extracted from an image corresponds to a quantum particle; each of these image-patches or potential surfaces with a quantum particle acts like a single-particle system.
- These single-particle systems are not isolated from each others, on the contrary, the interaction between them and other patches occurs within the whole image, like a quantum many-body system, where a particle-to-particle interaction takes place in the quantum system.
- As a consequence of these interactions, the effective potential (see (6)) of quantum particles changes, thus the local oscillation frequency of the wave function depends on these interactions.
- These interactions transmit structural features to the wave functions through the effective potential.
- The effective potentials will be used to construct an adaptive basis for each individual patch, in particular used for the decomposition of that patch.
- As an element of the set of oscillatory functions, this basis function uses low oscillation frequencies to probe higher values of the effective potential and vice-versa, *i.e.*, local frequencies depend on the effective potential, and thus on the pixel values and inter-patch interactions.

B. Denoising algorithm using quantum many-patch interactions

This subsection illustrates in detail the application of the proposed many-patch scheme to address image denoising. In this application, the construction of an adaptive basis for each individual image-patch is the primary objective, which leads to a three step denoising strategy: decomposition of that patch using the adaptive basis, thresholding of the projection coefficients, and finally recovery of the denoised patch by back-projection. These basis vectors are the eigenvectors of the Hamiltonian matrix (2), constructed from the effective potential (6).

These adaptive vectors belong to the Hilbert space of oscillatory functions with: i) the frequency of oscillation increases with increasing energy value (*i.e.*, eigenvalue in (7)), and ii) a given basis vector uses low oscillation frequencies to probe higher values of the effective potential and vice-versa. It is now assumed that the noise primarily rules the high-frequency components of the image, *i.e.*, eigenvectors corresponding to higher energy eigenvalues. Therefore as in the single-particle algorithm, thresholding in energy should be done to eliminate the image components associated with the high energy eigenvectors.

In the proposed interaction framework, the structural similarity between neighboring image patches is assumed to be an innate property of the image. Hence two neighboring patches are assumed to be similar to the extent of random noise. Following the definition (8), two adjacent patches show high interaction if they are pixel-wise dissimilar (*i.e.*, random noise is present), thus further contributing to the effective potential (6). In other words, the interaction term or ultimately the effective potential increases if the noise intensity increases, which eventually shifts the high-frequency noise components of the image to even higher energy eigenvectors. Thus, in order to have a denoised patch, a noisy patch is projected onto a d -dimensional subspace that is constructed by the lowest energy solutions of (7) and rebuild the denoised patch from these projection coefficients. In this way, a lack of similarity between pixels leads to a stronger denoising, since for the same value of the energy these regions will have lower frequencies than the ones with more similarity. Here, d acts as a thresholding hyperparameter. Combining all the denoised patches, following a similar path proposed in the non-local means architecture, one can obtain the final denoised image. Hereafter this proposed adaptive quantum denoiser which integrates the quantum theory of interactions to imaging problems is called Denoising by Quantum Interactive Patches (De-QuIP). The whole denoising process is regrouped



Fig. 3. Sample images (sizes in parentheses).

TABLE I

SIMULATION DATA WITH DIFFERENT PATCH SIZES FOR THE *Lake* IMAGE CONTAMINATED BY AWGN (SNR = 16DB). FOR THE PROPOSED DE-QUIP METHOD HYPERPARAMETERS $\hbar^2/2m = 1.5$, AND p AND d ARE ESTIMATED FROM THE EQUATIONS (9) AND (10) RESPECTIVELY.

	Data	1 × 1	3 × 3	5 × 5	7 × 7	11 × 11	17 × 17	27 × 27	63 × 63
QAB	PSNR(dB)	11.36	12.78	21.56	24.40	26.54	27.12	27.33	28.09
	SSIM	0.43	0.46	0.48	0.48	0.63	0.70	0.74	0.79
	Time(sec)	30.56	17.09	41.31	70.32	161.96	328.97	881.69	5800.72
De-QuIP	PSNR(dB)	22.12	28.16	28.73	28.84	28.58	28.23	28.16	27.77
	SSIM	0.37	0.78	0.83	0.83	0.82	0.81	0.80	0.79
	Time(sec)	21.93	22.75	82.61	108.01	490.52	3829.31	5644.90	22765.18

in Algorithm 1 in the Supplementary Material file.¹. The Computational complexity of the proposed algorithm is discussed in details in the Supp. Mat. file, see Section B.

IV. SIMULATION RESULTS

This section illustrates the interest of the proposed approach in image denoising problems and explores ways to choose the suitable hyperparameters. At the outset, Subsection IV-A explains the reliance of the proposed denoising scheme on the optimal choice of the hyperparameters P_h , W_h , p , $\hbar^2/2m$ and d , and explores rules for their possible estimations. For a thorough investigation, we explore cases of four different noise intensities (low to high) with image independent (*e.g.*, Gaussian) and dependent (*e.g.*, Poisson) noise models. The subsequent Subsection IV-B provides denoising results and a comparison between the proposed approach and several standard state-of-the-art methods. Finally, the section ends with a real medical application in Subsection V-F, which highlights the potential of the proposed scheme for the despeckling of real-world ultrasound (US) images.

A. Influence of hyperparameters P_h , W_h , p , $\hbar^2/2m$ and d and how to select them

1) *Effect of patch size P_h :* The localization of the basis vectors is associated with the length of the image patch, as explained in Subsection II-B5. The respective localization length or IPR decreases for increasing noise intensity. To deal with this quantum localization phenomenon, the size of the patch should be always less than or equal to the localization length of the basis vectors for different levels of noise. If the localization length is greater than the size of the patch, the basis vectors probe the entire region of the image patch with different ranges of oscillation frequencies depending on the intensity of the image pixels. On the contrary, a smaller localization length leads to an exponential localization of the basis vectors on a specific part of the image patch. Thus, these localized vectors will not have different frequencies at different pixel values and lose a key asset of this formalism. The drastic effect of this localization phenomenon on image denoising is shown in our previous work [35], where an additional Gaussian smoothing was necessary before computing the quantum adaptive basis (QAB), used as a denoiser in that process. On the contrary, the current formalism eliminates this issue without any additional computational requirements.

Furthermore, a smaller patch size helps to reduce the computational complexity, as discussed in the section above. As a consequence, De-QuIP denoiser is more computationally efficient than the previously proposed QAB denoiser in [35]. Table I summarizes the run time using the QAB and De-QuIP denoiser with increasing patch size. The peak signal to noise ratios (PSNR) and the structure similarity (SSIM), used as denoising quality metrics, are given to have a quantitative analysis concerning the patch size. All the algorithms have been implemented in Matlab and tested on a computer with an Intel(R) Core(TM) i7-10510U CPU of 4 cores each with 1.80 GHz, 16 GB memory and using Windows 10 Pro version 20H2 as operating system. From Table I, one can see that the computational time for both denoisers increases as the patch size increases but the denoising performance (*i.e.*, PSNR and SSIM values) for De-QuIP first increases with the patch size and then begins to decrease gradually after size 11×11 . Whereas, QAB requires much larger patches to achieve a similar performance, which essentially imposes a huge computational burden on the process. The gradual decrease in the performance of the De-QuIP denoiser for increasing patch size is expected due to the localization phenomenon, which is discussed above. Therefore, a smaller patch size preserves the fundamental features of these adaptive vectors and reduces the computational complexity and run time. Herein, we will only focus on the patch sizes 5×5 , 7×7 and 11×11 for further investigations.

¹The Matlab code of the proposed denoising algorithm is available at github.com/SayantanDutta95/

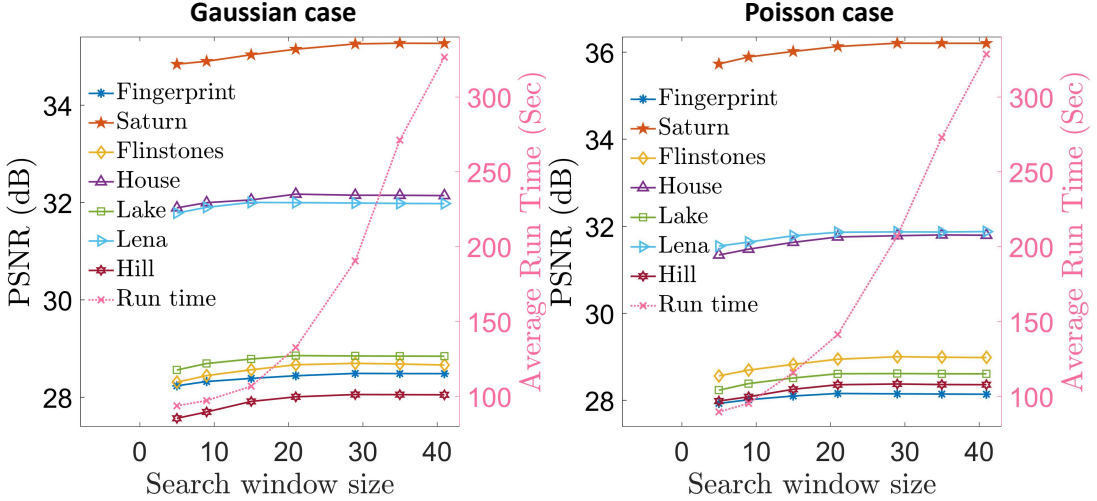


Fig. 4. Denoising performance in terms of PSNR (left y-axis) and average run time (right y-axis) of De-QuIP as a function of the search window size for the first seven sample images in Fig. 3. The images hyperparameters $P_h = 7$ and others are estimated from the eq. (9)–(12).

2) *Effect of the search window size W_h :* The search window is the image region around the current patch regrouping all the patches interacting with it. Following the discussion in Subsection II-B3, the size of the search window plays an important role in preserving the structural similarities in a local neighborhood. This search window is usually defined as a square window of limited size so that the implementation is restricted to a small neighborhood centered on the target patch (to be denoised) instead of the whole image. In the literature, mostly two types of approaches are used, based on a fixed search window size [16]–[18], [23] or an adaptive approach [21]. In this work, we concentrate on the fixed size approach for examining the effect of the search window on De-QuIP.

Fig. 4 shows the denoising performance of De-QuIP in terms of PSNR as a function of the search window size for the Gaussian and Poisson noise cases. For these simulations, the patch size is kept fixed at 7×7 for all images. Note that in these simulations patches overlap, given that consecutive target patches are one pixel away from each other, both in the horizontal and vertical direction. In Fig. 4, one can see that in both cases, the denoising ability increases with the size of the search window before roughly stabilizing beyond a size 20×20 for both noise models. These observations show that the patch neighborhood is important to increase the denoising performance but larger search windows do not bring additional information about the neighborhood due to the inverse square nature of the interaction term. It is also important to notice that the computation time increases with the search window size, as shown in the right y-axis in Fig. 4. The use of a relatively moderate size search window is computationally more efficient while preserving the image attributes using the proposed interaction framework. Note that these results are consistent for other patch sizes. Therefore, for simplicity, in this work we choose a search window size of 15×15 , 21×21 and 33×33 respectively for the patch sizes of 5×5 , 7×7 and 11×11 . One interesting observation can be drawn here, that the search window size changes with the patch size and not with the noise model within the proposed algorithm.

3) *Influence of the proportionality constant p :* As mentioned above, the proportionality constant p regulates the interaction term in the effective potential, and consequently the shape of the basis vectors. Hence, there exists an optimal choice of p depending on the size of the patch for optimal performance of De-QuIP for a given noisy image. Fig. 5(a) presents the denoising performance in terms of PSNR as a function of p for the *house* image corrupted with AWGN (SNR = 16dB), for three different patch sizes. These optimal values also depend on the level of noise present in the image. These p values that maximize the output PSNRs for the first seven sample images corrupted with different noise intensities are highlighted in Fig. 3. These optimal p values are shown as a function of SNR in Fig. 6 using box-plots for a fixed patch size. The observations confirm that there is a tendency for optimal values to decrease as the noise level increases. For explicit details of these optimal values, we refer readers to the Supp. Mat. file Section C. A possible explanation for this phenomenon comes from the fact that dissimilarities increase with the noise intensity in a local-neighborhood. Hence, to balance the original potential (patch pixels) and the interactions in the effective potential, the hyperparameter p decreases.

The data in Fig. 6 enables rules to fix the p value closer to its optimal values. The distribution of the data gives an intuition about a possible linear relationship between the optimal p and the SNR. Therefore, the proportionality constant p can be chosen from the following rule:

$$p = m_1 \times (\text{SNR}) + c_1. \quad (9)$$

In Fig. 6, the best linear fits to the optimal p as a function of SNR are shown for three different patch sizes as well as for Gaussian and Poisson noise models. These linear fits give a robust way of choosing the suitable p for a given patch size and

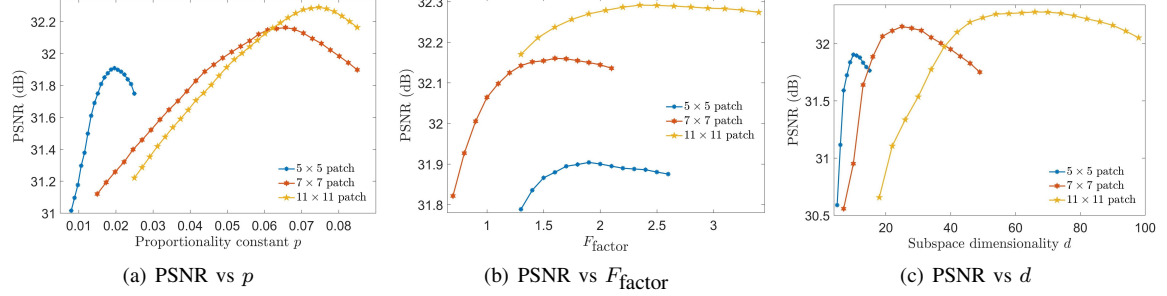


Fig. 5. Denoising performance of De-QuIP in terms of PSNR as a function of the hyperparameters for the *house* image corrupted with AWGN (SNR = 16dB) using three different patch sizes. All hyperparameters are estimated using equations (9)-(12).

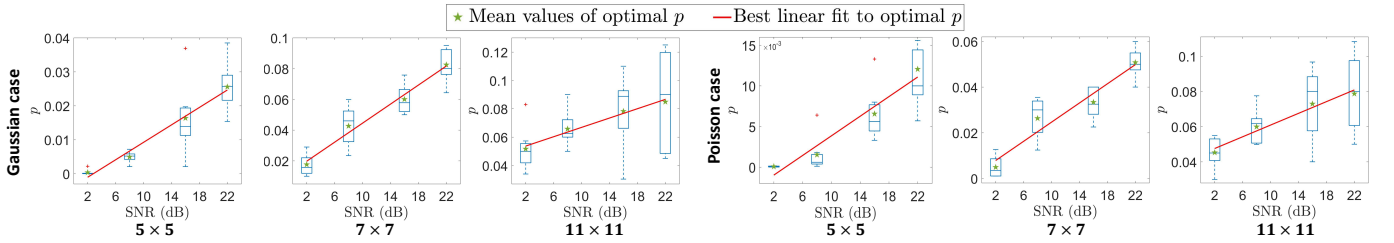


Fig. 6. Optimal proportionality constant p value as a function of SNR for three patch sizes, where the three left and the three right graphs are associated with the case of Gaussian and Poisson noise models. The bars indicate the minimum and maximum values of the optimal p . The bottom and top edges of the blue boxes indicate the 25th and 75th percentiles and the central mark and green star indicate the median and mean values. The red line is the best linear curve fitted to the data points corresponding to the mean of the optimal p values.

noise level.

The linear fit parameters are summarized in the Supp. Mat. file Section C together with the ℓ_2 error and the resulting average loss in the denoising performance in terms of PSNR and SSIM. One may notice that the denoising performance loss with rule (9) rather than the optimal choice is negligible. This is expected due to the smooth nature of the PSNR curve with a broad maxima shown in Fig. 5(a), which makes the De-QuIP resilient to small sub-optimalities in the adoption of p . Hence, it is anticipated that the parameters learned from the sample images to estimate p using (9), will be effective for a large set of images. These conclusions are valid for various cases of noise models and patch sizes, as shown in the simulations results. Furthermore, an adaptive approach of tuning p that depends on the image patch gives an alternative to the above rules and opens an interesting perspective for future investigation.

4) *Influence of the $\hbar^2/2m$ and subspace dimensionality d :* The last two hyperparameters to be analyzed are $\hbar^2/2m$ and the subspace dimensionality d . Although the utilization of these two hyperparameters seems to be different, the first one being used in the construction of the Hamiltonian operator and the other one acting as a threshold, there is a deep connection between them. In this subsection, we will explain this connection with experimental validation and propose rules for automated estimation of their optimal choices.

As stated above in Subsection II-A1, the hyperparameter $\hbar^2/2m$ controls how the local frequencies of the basis vectors change with the image pixel values. For low values of $\hbar^2/2m$, the oscillation frequencies are very high, regardless of the low and high pixel values, due to the presence of a very high maximal oscillation in this limit which restricts the wave vectors from properly exploring higher pixel values. On the other side, increasing too much the values of $\hbar^2/2m$ decreases the ability of the basis vectors to distinguish between high and low values pixels. For more illustrations about the effect of this hyperparameter $\hbar^2/2m$ on the basis vectors, we refer readers to our previous work [35]. Therefore, the optimal $\hbar^2/2m$ value has a strong dependence on the maximum and minimum values of the pixels present in the image patch. Thus, it is more convenient to use an adaptive way to select $\hbar^2/2m$ that depends on the image patch to have the optimal performance of De-QuIP. Herein, it is possible to write the hyperparameter in terms of the difference between this maximum and minimum pixel values multiplied by a factor F_{factor} , for example, for the patch A ,

$$\hbar^2/2m = F_{\text{factor}} \times (A_{\max} - A_{\min}), \quad (10)$$

where A_{\max} , A_{\min} are the maximum and minimum pixel values of the patch A . Hence, the optimal choice of F_{factor} is needed to have the best possible output.

In this proposed scheme, the subspace dimensionality d is used as the threshold for truncating high energy wave solutions, which mostly carry noise information. Hence, an optimal choice of d exists for a noisy image that yields the best denoising output depending on the patch size. $\hbar^2/2m$ or say F_{factor} controls the frequency distribution across the basis vectors since

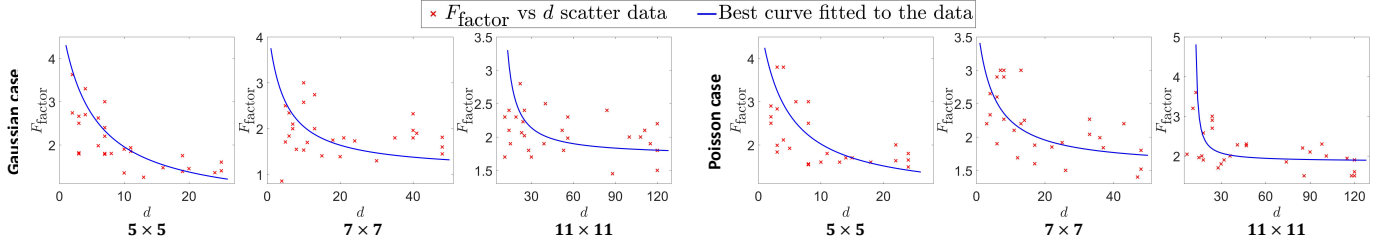


Fig. 7. F_{factor} vs d scatter plot and the respective best-fitted curve of the form $(F_{\text{factor}} - l_1) = l_3/(d - l_2)$.

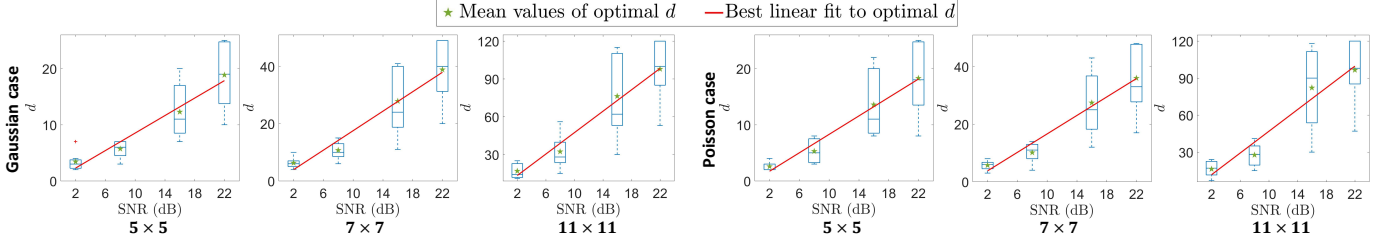


Fig. 8. Optimal subspace dimensionality d value as a function of SNR for three patch sizes are shown for the Gaussian and Poisson noise models. Similar to Fig. 6, a box-plot diagram is used for the optimal d . The red line is the best linear curve fitted to the data points corresponding to the mean of the optimal d .

the maximal frequency of a vector with energy E at the local pixel value V is $\sqrt{(E - V)/(h^2/2m)}$. Hence, the maximal frequency decreases with increasing F_{factor} . As a consequence, low-energy basis vectors become more prominent to distinguish low and high pixel regions using different levels of frequency. Thus, the optimal subspace dimensionality d decreases as F_{factor} increases. These optimal choices vary with the image patch size and noise statistics. In Fig. 7, all these optimal values that give the best output PSNRs for the first seven sample images are shown as a scatter-plot of F_{factor} vs d , which clearly shows their inverse relationship, *i.e.*, d decreases with F_{factor} 's growth or vice-versa and validates our above arguments. More details of these optimal values can be found in the Supp. Mat. file Section D.

These experimental data enable an automated way of selecting the values of d and F_{factor} close to their optimalities. To do this, the optimal d values are shown in Fig. 8 as a function of SNR using box-plots for a fixed patch size, for the Gaussian and Poisson cases. The observation shows a very predictable behaviour of this optimal d as a function of SNR which is expected as it needs to be further thresholded as the noise increases. For a specific patch size, the optimal d and SNR follow a linear relationship. Therefore, the subspace dimensionality d and F_{factor} can be inferred from the following two rules,

$$d = m_2 \times (\text{SNR}) + c_2, \quad (11)$$

$$F_{\text{factor}} - l_1 = l_3/(d - l_2). \quad (12)$$

Figs. 7 and Fig. 8 show the best-fitted curves to the optimal F_{factor} and d , and the respective fit parameters are regrouped in the Supp. Mat. file Section D. These rules give an efficient way of selecting the hyperparameters close to their optimality depending on the size of the given patch and the intensity of the noise. Our data show that the respective costs in terms of performance loss are minimal, since the output PSNR curves are smooth and have broad maxima, shown in Fig. 5(b)-5(c) for the choice of F_{factor} and d , as discussed in Subsection IV-A3 for the hyperparameter p . Hence, the rules for automated selecting hyperparameters are expected to be valid for other images as well.

B. Denoising efficiency of the proposed scheme in comparison with standard methods

This subsection presents the denoising performance of the De-QuIP algorithm depending on the noise statistics and intensity, and also how this performance varies with patch size for the sample images. The denoising outputs using three patch sizes are summarized in the Supp. Mat. file, see Section E. The numerical simulations show that 11×11 is the suitable patch size for most of the cases, but for low-level noise, smaller sizes give a small advantage. It is expected to have a better result with a large patch for a strong noise scenario since high noise intensity refers to an extreme random system and a large patch is more efficient to capture the similarity measures from this strong randomness. Obviously, the size should not be so large because it is affected by the phenomenon of localization, as illustrated in Subsection II-B5.

As explained earlier, the De-QuIP follows a similar principle to the NLM approach. Comparisons with NLM-based state-of-the-art methods are thus provided in order to prove the efficiency of the proposed algorithm. However, for a comprehensive survey of the denoising ability of De-QuIP, rigorous comparisons with contemporary noise removal methods from the literature are also presented. For the recovery of Gaussian corrupted images, the following methods were used for comparison: NLM

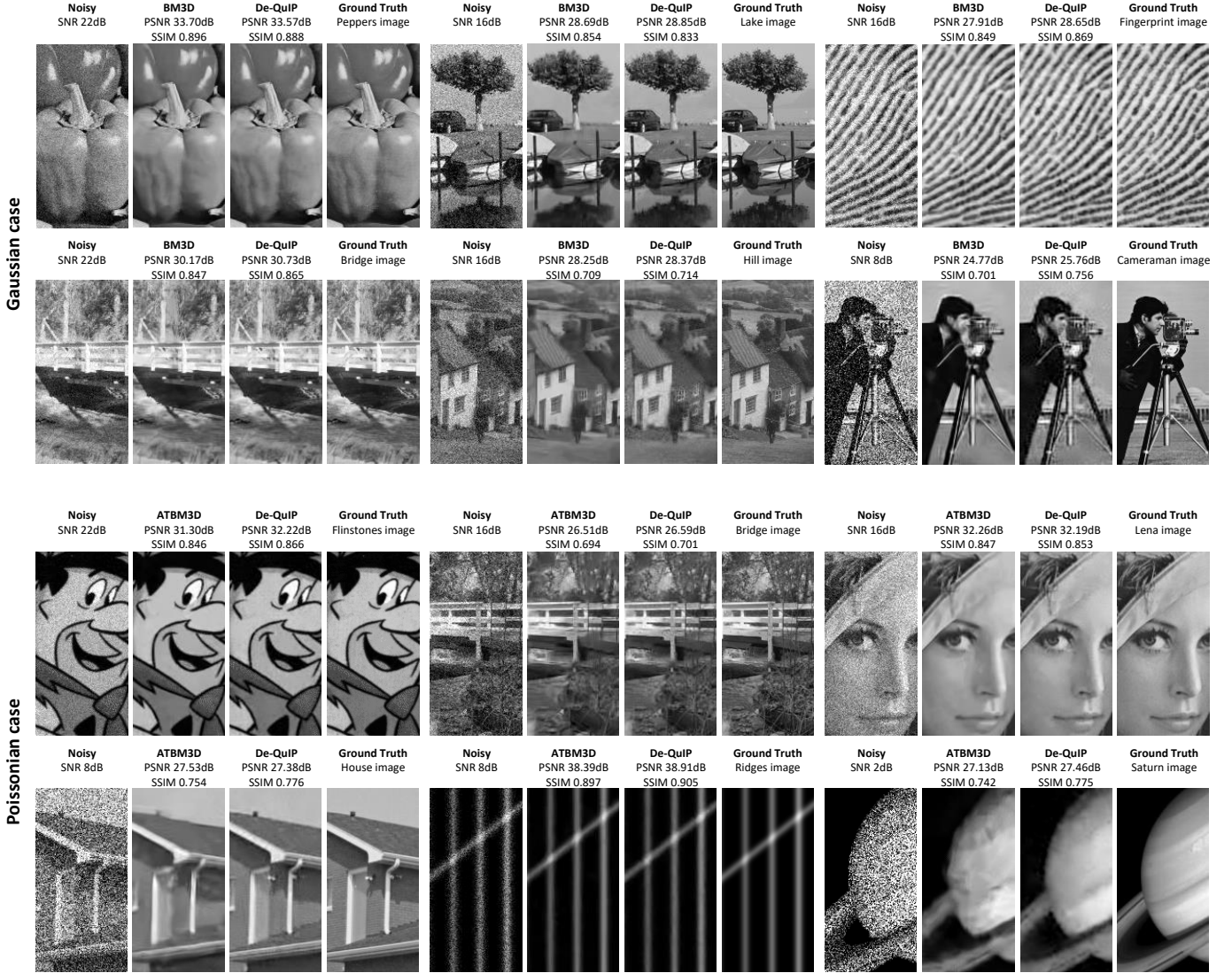


Fig. 9. The top two and bottom two rows depict the Gaussian and Poissonian denoising results, respectively. The noisy, BM3D-based results, De-QuIP results, and ground-truth images are presented here accordingly. The BM3D-based and De-QuIP schemes are listed as these are always among the two best-performing methods.

method using PCA called PND in [16], two patch-based PCA for NLM denoising methods referred to as PGPCA (global approach) and PLPCA (local approach) in [17], BM3D [13], dictionary learning (DL) method [12], graph signal processing (GSP) method [6], and finally, our earlier implementations of quantum adaptive basis (QAB) for image denoising based on the single particle theory [35].

For the recovery of Poisson corrupted images, comparisons have been carried out with recent algorithms dedicated to the Poissonian model such as Poisson non-local PCA (PNLPCA) [46], BM3D consolidated with the Anscombe transform [47] leveled as ATBM3D, and finally the QAB [35] method.

The proposed denoising algorithm has been extensively compared to other standard methods to demonstrate the accuracy of De-QuIP. Detailed quantitative evaluations in terms of PSNR and SSIM for both noise models are available in the Supp. Mat. file, see Section E. From these results, one can observe that De-QuIP scheme significantly outperforms all NLM-based methods with an average gain of 1.1 to 2.6 dB in PSNR and 3 to 20% in SSIM. One can also observe that De-QuIP and BM3D-based methods stand out as the two best-performing algorithms for both Gaussian and Poissonian cases. The denoising performance of De-QuIP and BM3D-based methods are presented in Fig. 9 for visual inspection, where ground truth, noisy, and corresponding denoised images are shown. These results confirm the good performance of De-QuIP regardless of the noise model and intensity. In the denoised images, image features and details, for example, patterns (in *Fingerprint* and *Ridges*), sharp edges (in *Lake*, *Bridge*, *Cameraman* and *House*), smooth areas (in *Peppers*, *Flintstones*, and *Lena*), are well-preserved. Although BM3D and respectively ATBM3D are slightly more accurate in some of the experiments, a smoothing effect is present in their corresponding denoised images and becomes more prominent as the noise level increases. This effect is clearly

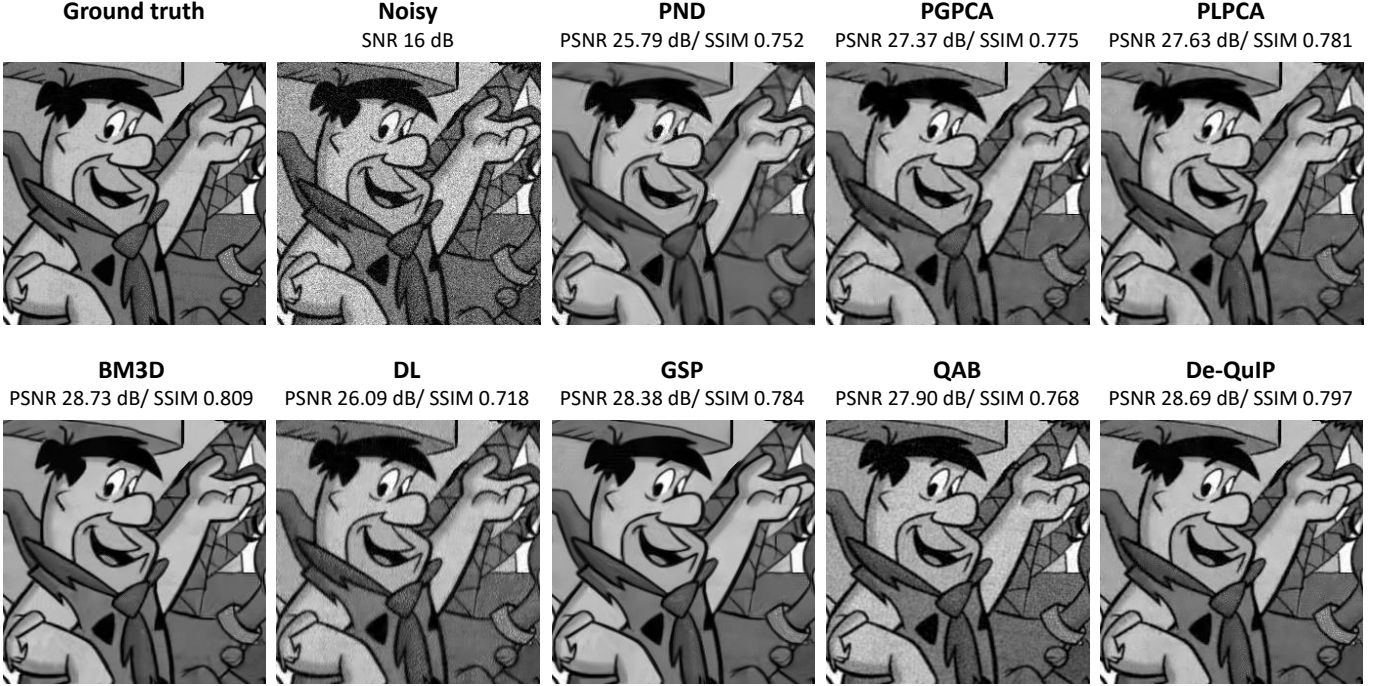


Fig. 10. Zoomed segments of the denoised estimations of the *Flintstones* image while corrupted with AWGN (SNR 16dB) using different methods.

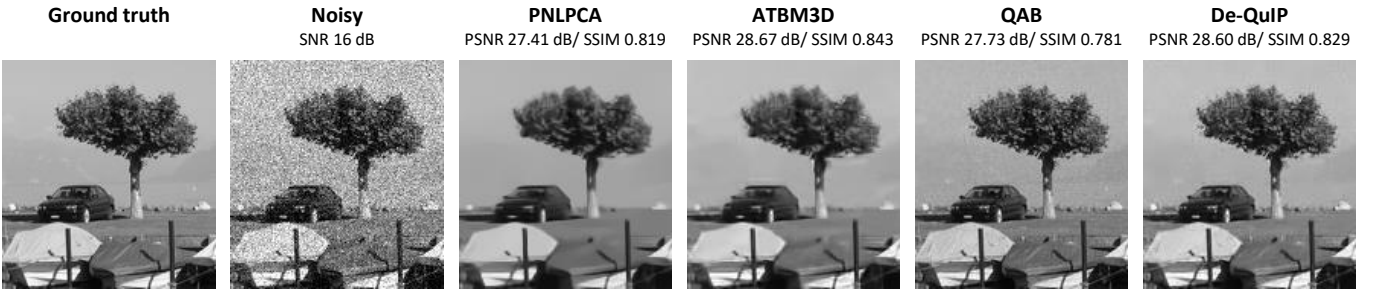


Fig. 11. Zoomed segments of the denoised estimations of the *Lake* image while corrupted with Poisson noise (SNR 16dB) using different methods.

visible around the windows and roof of the *Hill*, on the patterns of the *Fingerprint*, near the eye of the *Lena*, on the face of the *Flintstones*, and around the sharp edges of the *House* images, while De-QuIP preserves all these image features in a better way and consequently provides a denoised image closer to the original one. This is due to the interaction term that allows De-QuIP to better extract the image information. Although, for the increasing noise intensity, some artefacts can be observed in the denoised images (for example in *House*, *Saturn*, *Cameraman* images) due to the presence of strong noise, they are very few and negligible for low-level noises.

For further inspection in Fig. 10, we show zoomed segments of the denoised results of the *Flintstones* image while corrupted with AWGN (SNR 16dB). Similarly, for Poisson corrupted (SNR 16dB) *Lake* image the zoomed segments of the denoised estimations are shown in Fig. 11. Quantitative performance in terms of PSNR and SSIM adopting different methods for Gaussian and Poisson contaminated images are presented in Fig. 12 using box-plots as a function of SNR. Readers may refer to the Supp. Mat. file to have more details related to these experiments.

Through visual and quantitative inspections of Figs. 10-11, it is clear that the proposed De-QuIP uniformly outperforms all the NLM-based approaches with a significant increase in terms of PSNR and SSIM. For Gaussian corrupted images, BM3D is still the best method in most cases, but De-QuIP allows competitive comparisons in all scenarios. Furthermore, for both noise models, the positive effects of local similarity considerations are clearly visible in the Fig. 12 data of QAB and De-QuIP, as it gives much better PSNR and SSIM values with significantly fewer computations. The Figs. 10-11 show a pronounced gain in the qualitative performance of the proposed DeQuIP model against the QAB. Therefore, exploiting the structural details through interaction terms notably contributes to the preservation of image details, as conveyed by quantitative and visual assessments. Additionally, regardless of the noise intensity, De-QuIP always provides good PSNR and SSIM for the recovery of Gaussian corrupted images as shown in Fig 12(a), which is not the case with most algorithms, as highlighted by SSIM values. Although

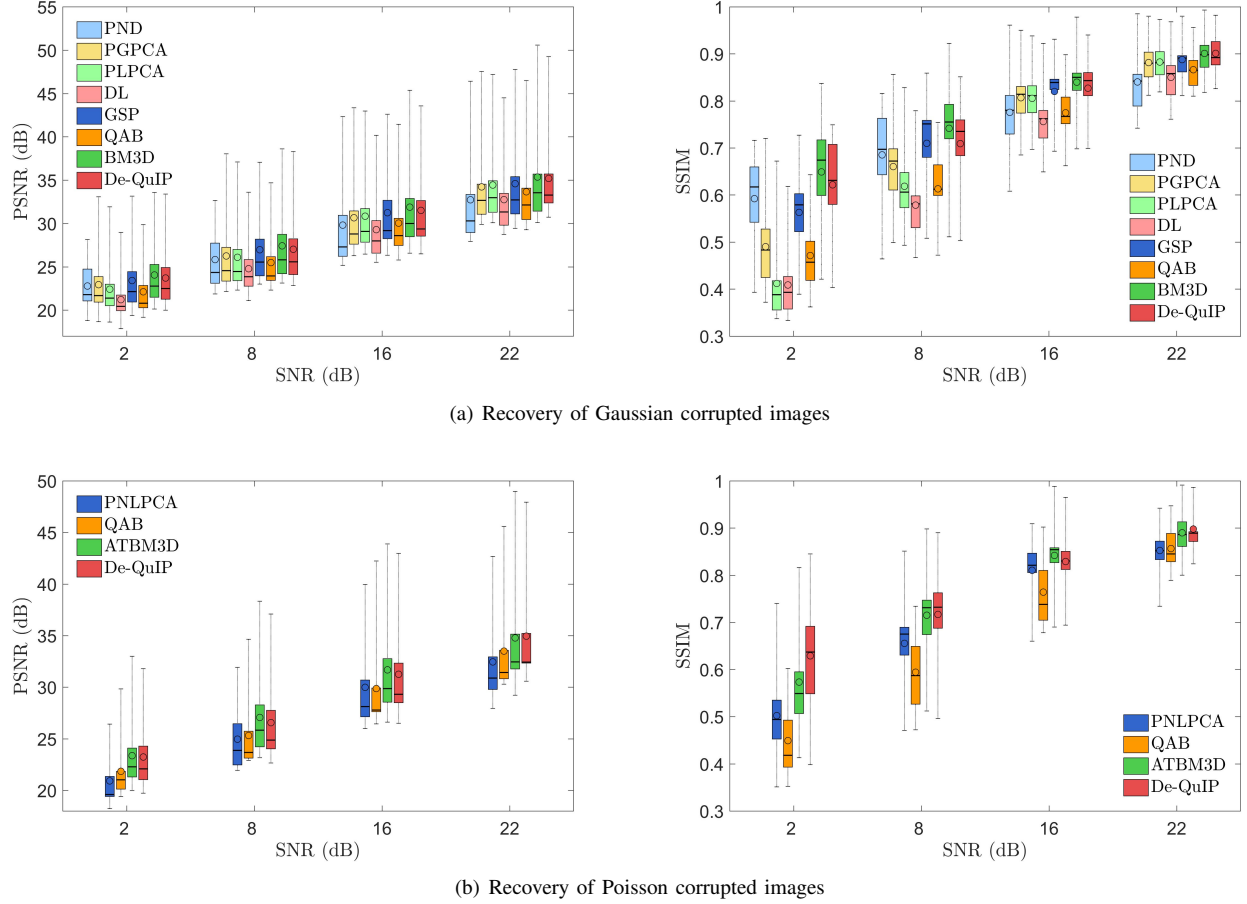


Fig. 12. Quantitative denoising results using different methods for Gaussian and Poisson corrupted images with four different noise levels. The bottom and top edges of the boxes indicate the 25th and 75th percentiles, and the central black line and circle indicate the median and mean relative to the data points.

in Fig. 12(a), our results look comparable with BM3D, one should note that a beautification happens in the BM3D outputs due to the smoothing effect as illustrated in Fig. 9, which is not present in our outcomes and makes our resultant image texture closer to the original one.

For Poisson corrupted images, De-QuIP provides better outcomes compared to the other methods. ATBM3D generates comparable PSNR and SSIM data in some scenarios, but the visual assessment clearly shows an extra smoothing effect present on the denoised image, which causes lower SSIM values for low SNR images as shown in Fig. 12(b). This is due to the process of data Gaussianization through the Anscombe transformation. In addition, for increasing noise intensity, this Anscombe transformation loses its accuracy [36], which is clearly observable in the Fig. 12(b) in the cases of low SNR. On contrary, De-QuIP is a straightforward method without having any such transformation and efficiently shows good denoising performance in all situations. Similar to the Gaussian case, De-QuIP outperforms PNLPCA, a NLM based method, by a large margin. This proves its adaptability for high as well as for low SNR images regardless of their noise statistics which can be viewed as a strong point in several practical applications.

C. Application to ultrasound (US) image despeckling

In this subsection, for further illustration of the potential of De-QuIP, we investigated its ability for real medical US image despeckling. US imaging is an integral part of modern medical science as it gives harmless, non-invasive, real-time images in an affordable way. The main artefact affecting US images is a random granular pattern, the speckle, which is generated by random constructive and destructive interference between US waves. This phenomenon related to the acquisition system is used as a source of information about the tissues in several applications, but can also affect the interpretability of the images by diminishing their readability. Indeed, the speckle does not follow an additive rule and has a complex noise distribution. Therefore, the important task of estimating speckle-free US images, known as despeckling [48] in the relevant literature, has been extensively explored using various schemes [49]–[52] to enhance the readability of the US images.

Despeckling performance of De-QuIP is investigated through a phantom as well as four real cancer and two non-cancer thyroid US images acquired with a 7.5 MHz linear probe. As an extension of our preliminary results in [53], we are proposing

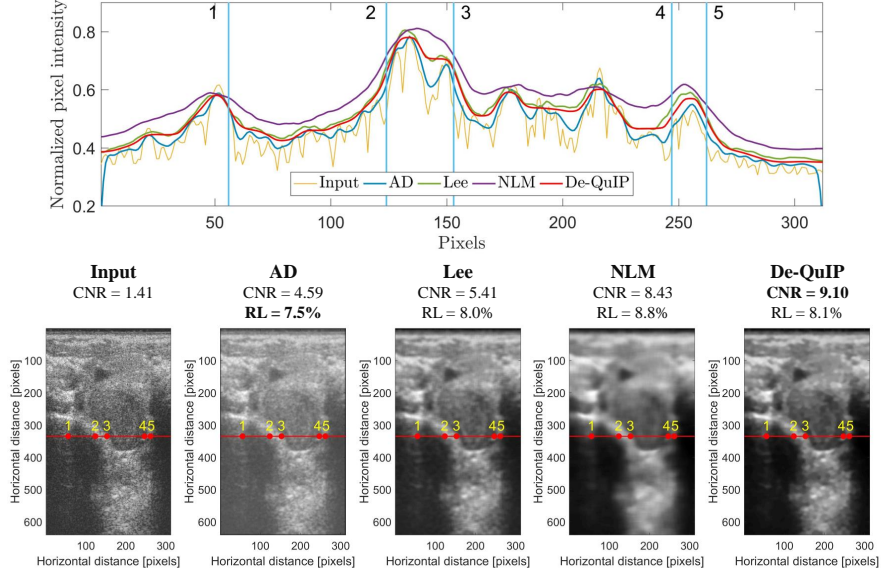


Fig. 13. US image despeckling results using different methods for cancer thyroid image. The normalized pixel intensities of the extracted red lines from speckled and despeckled US images are shown.

a comprehensive study of this problem here. The estimated despeckled outcomes are compared with three existing despeckling algorithms, the anisotropic diffusion (AD) [49], Lee [52] and NLM [16] filters. For the quantitative analysis, the contrast-to-noise-ratio (CNR) and resolution loss (RL) are regrouped for a cancer image with visual demonstrations in Fig. 13. Observation shows that De-QuIP offers a better image contrast (higher CNR than AD, Lee and slightly lower than NLM, which over-smooths the images and yields poor resolution) while having less spatial resolution loss (De-QuIP has less spatial resolution loss compared to the native US image). Note that these images are chosen arbitrarily, that is, the quality of the results should not depend on the data tested. More data related to these experiments can be found in the Supp. Mat. file, see Section F.

V. CONCLUSIONS AND PERSPECTIVES

A novel image denoising algorithm inspired by the quantum many-body theory has been developed in this paper. This gives a way to adapt the concept of interaction from the many-body physics to an imaging problem. More precisely, the interactions between image patches are nothing more than a reflection of the similarity-measures in a local image neighborhood and provide an efficient way to capture the local structures of real images. Through these interactions, structural details are transmitted on a patch-based adaptive basis created by the solutions of the Schrödinger equation of quantum mechanics, which can be exploited as filters for denoising the patches. The versatile nature of the adaptive basis that conveys the structural similarities of image neighborhood, extends its scope of applications beyond AWGN without modification.

A rigorous comparison with contemporary methods exemplifies the denoising ability of our De-QuIP algorithm regardless of the image nature, noise statistics and intensity. Simulation results demonstrate that the proposed method clearly outperforms other schemes and gives a good comparison with the best outcome for both image independent and dependent noise models. Additionally, De-QuIP achieves much better results at a significantly less computational cost in comparison with the earlier single-particle based quantum scheme of e.g. [35]. To make De-QuIP more robust, automated rules are discussed in the paper to efficiently select the values of the hyperparameters close to the optimal ones when less information is available. Furthermore, its good performance in real-life medical US image despeckling applications further shows its ability in handling multiplicative noise efficiently.

Adaptation of this new quantum many-body idea opens up a new domain of future explorations. Since De-QuIP primarily has a non-local nature and significantly outperforms contemporary NLM-based methods, the first obvious perspective comes from the extension of this idea of interactions for collaborative patch denoising, as originally proposed in [13].

A second interesting point would be to embed this interaction architecture into a convolutional neural network, as explored with various schemes, such as a fast flexible learning method [54], [55], residual learning [56] and others, and study imaging problems through this many-body network where each node shows interaction with others.

Another possibility is to use a more advanced theory of physics, such as the time-dependent Schrödinger equation, a fascinating perspective for further research.

Further expansion of the framework in three dimensional data or RGB color images can be easily done by simply bypassing data across different processing channels. Finally, other imaging applications, such as deconvolution or super-resolution, could also take benefit of this interaction model.

ACKNOWLEDGMENTS

This work was supported in part by Centre National de la Recherche Scientifique (CNRS) through the 80 Prime Program.

REFERENCES

- [1] A. Hamza, H. Krim, Image denoising: a nonlinear robust statistical approach, *IEEE Trans. Signal Process.* 49 (12) (2001) 3045–3054. [doi:10.1109/78.969512](https://doi.org/10.1109/78.969512).
- [2] A. Pizurica, W. Philips, Estimating the probability of the presence of a signal of interest in multiresolution single- and multiband image denoising, *IEEE Trans. Image Process.* 15 (3) (2006) 654–665. [doi:10.1109/TIP.2005.863698](https://doi.org/10.1109/TIP.2005.863698).
- [3] M. Lebrun, A. Buades, J. Morel, A nonlocal bayesian image denoising algorithm, *SIAM J. Imag. Sci.* 6 (3) (2013) 1665–1688. [doi:10.1137/120874989](https://doi.org/10.1137/120874989).
- [4] D. Shuman, S. Narang, P. Frossard, A. Ortega, P. Vandergheynst, The emerging field of signal processing on graphs: Extending high-dimensional data analysis to networks and other irregular domains, *IEEE Signal Process. Mag.* 30 (3) (2013) 83–98. [doi:10.1109/MSP.2012.2235192](https://doi.org/10.1109/MSP.2012.2235192).
- [5] A. Sandryhaila, J. Moura, Discrete signal processing on graphs, *IEEE Trans. Signal Process.* 61 (7) (2013) 1644–1656. [doi:10.1109/TSP.2013.2238935](https://doi.org/10.1109/TSP.2013.2238935).
- [6] J. Pang, G. Cheung, Graph laplacian regularization for image denoising: Analysis in the continuous domain, *IEEE Trans. Image Process.* 26 (4) (2017) 1770–1785. [doi:10.1109/TIP.2017.2651400](https://doi.org/10.1109/TIP.2017.2651400).
- [7] S. Kim, Pde-based image restoration: a hybrid model and color image denoising, *IEEE Trans. Image Process.* 15 (5) (2006) 1163–1170. [doi:10.1109/TIP.2005.864184](https://doi.org/10.1109/TIP.2005.864184).
- [8] P. Liu, F. Huang, G. Li, Z. Liu, Remote-sensing image denoising using partial differential equations and auxiliary images as priors, *IEEE Geosci. Remote Sens. Lett.* 9 (3) (2012) 358–362. [doi:10.1109/LGRS.2011.2168598](https://doi.org/10.1109/LGRS.2011.2168598).
- [9] D. Donoho, I. Johnstone, Ideal spatial adaptation by wavelet shrinkage, *Biometrika* 81 (3) (1994) 425–455. [doi:10.1093/biomet/81.3.425](https://doi.org/10.1093/biomet/81.3.425).
- [10] J.-L. Starck, E. Candes, D. Donoho, The curvelet transform for image denoising, *IEEE Trans. Image Process.* 11 (6) (2002) 670–684. [doi:10.1109/TIP.2002.1014998](https://doi.org/10.1109/TIP.2002.1014998).
- [11] M. Aharon, M. Elad, A. Bruckstein, K-svd: An algorithm for designing overcomplete dictionaries for sparse representation, *IEEE Trans. Signal Process.* 54 (11) (2006) 4311–4322. [doi:10.1109/TSP.2006.881199](https://doi.org/10.1109/TSP.2006.881199).
- [12] M. Elad, M. Aharon, Image denoising via sparse and redundant representations over learned dictionaries, *IEEE Trans. Image Process.* 15 (12) (2006) 3736–3745. [doi:10.1109/TIP.2006.881969](https://doi.org/10.1109/TIP.2006.881969).
- [13] K. Dabov, A. Foi, V. Katkovnik, K. Egiazarian, Image denoising by sparse 3-d transform-domain collaborative filtering, *IEEE Trans. Image Process.* 16 (8) (2007) 2080–2095. [doi:10.1109/TIP.2007.901238](https://doi.org/10.1109/TIP.2007.901238).
- [14] K. Dabov, A. Foi, V. Katkovnik, K. Egiazarian, Bm3d image denoising with shape-adaptive principal component analysis, in: Proc. Signal Process. Adapt. Sparse Struct. Represent. (SPARS), 2009, pp. 1–7.
- [15] A. Buades, B. Coll, J.-M. Morel, A review of image denoising algorithms, with a new one, *SIAM Multiscale Model. Simul.* 4 (2) (2005) 490–530. [doi:10.1137/040616024](https://doi.org/10.1137/040616024).
- [16] T. Tasdizen, Principal neighborhood dictionaries for nonlocal means image denoising, *IEEE Trans. Image Process.* 18 (12) (2009) 2649–2660. [doi:10.1109/TIP.2009.2028259](https://doi.org/10.1109/TIP.2009.2028259).
- [17] C.-A. Deledalle, J. Salmon, A. Dalalyan, Image denoising with patch based pca: local versus global, in: Proc. BMVC, Vol. 81, 2011, pp. 425–455.
- [18] R. Vignesh, B. Oh, C.-C. Kuo, Fast non-local means (nlm) computation with probabilistic early termination, *IEEE Signal Process. Lett.* 17 (3) (2010) 277–280. [doi:10.1109/LSP.2009.2038956](https://doi.org/10.1109/LSP.2009.2038956).
- [19] C. Zuo, L. Jovanov, B. Goossens, H. Luong, W. Philips, Y. Liu, M. Zhang, Image denoising using quadtree-based nonlocal means with locally adaptive principal component analysis, *IEEE Signal Process. Lett.* 23 (4) (2016) 434–438. [doi:10.1109/LSP.2016.2530406](https://doi.org/10.1109/LSP.2016.2530406).
- [20] I. Frosio, J. Kautz, Statistical nearest neighbors for image denoising, *IEEE Trans. Image Process.* 28 (2) (2019) 723–738. [doi:10.1109/TIP.2018.2869685](https://doi.org/10.1109/TIP.2018.2869685).
- [21] C. Kervrann, J. Boulanger, Optimal spatial adaptation for patch-based image denoising, *IEEE Trans. Image Process.* 15 (10) (2006) 2866–2878. [doi:10.1109/TIP.2006.877529](https://doi.org/10.1109/TIP.2006.877529).
- [22] P. Chatterjee, P. Milanfar, Patch-based near-optimal image denoising, *IEEE Trans. Image Process.* 21 (4) (2012) 1635–1649. [doi:10.1109/TIP.2011.2172799](https://doi.org/10.1109/TIP.2011.2172799).
- [23] M. Mahmoudi, G. Sapiro, Fast image and video denoising via nonlocal means of similar neighborhoods, *IEEE Signal Process. Lett.* 12 (12) (2005) 839–842. [doi:10.1109/LSP.2005.859509](https://doi.org/10.1109/LSP.2005.859509).
- [24] D. Van De Ville, M. Kocher, Sure-based non-local means, *IEEE Signal Process. Lett.* 16 (11) (2009) 973–976. [doi:10.1109/LSP.2009.2027669](https://doi.org/10.1109/LSP.2009.2027669).
- [25] W. Dong, L. Zhang, G. Shi, X. Li, Nonlocally centralized sparse representation for image restoration, *IEEE Trans. Image Process.* 22 (4) (2013) 1620–1630. [doi:10.1109/TIP.2012.2235847](https://doi.org/10.1109/TIP.2012.2235847).
- [26] F. Li, Y. Ru, X. Lv, **Patch-based weighted scad prior for rician noise removal**, *J. Sci. Comput.* 90 (26) (2021) 1573–7691. [doi:10.1007/s10915-021-01688-5](https://doi.org/10.1007/s10915-021-01688-5)
URL <https://doi.org/10.1007/s10915-021-01688-5>
- [27] Z. Zha, X. Yuan, B. Wen, J. Zhou, J. Zhang, C. Zhu, From rank estimation to rank approximation: Rank residual constraint for image restoration, *IEEE Trans. Image Process.* 29 (2020) 3254–3269. [doi:10.1109/TIP.2019.2958309](https://doi.org/10.1109/TIP.2019.2958309).
- [28] Z. Zha, X. Yuan, J. Zhou, C. Zhu, B. Wen, Image restoration via simultaneous nonlocal self-similarity priors, *IEEE Trans. Image Process.* 29 (2020) 8561–8576. [doi:10.1109/TIP.2020.3015545](https://doi.org/10.1109/TIP.2020.3015545).
- [29] Z. Zha, B. Wen, X. Yuan, J. Zhou, C. Zhu, Image restoration via reconciliation of group sparsity and low-rank models, *IEEE Trans. Image Process.* 30 (2021) 5223–5238. [doi:10.1109/TIP.2021.3078329](https://doi.org/10.1109/TIP.2021.3078329).
- [30] Z. Zha, X. Yuan, B. Wen, J. Zhang, C. Zhu, Nonconvex structural sparsity residual constraint for image restoration, *IEEE Trans. Cyber.* (2021) 1–14 [doi:10.1109/TCYB.2021.3084931](https://doi.org/10.1109/TCYB.2021.3084931).
- [31] Ç. Aytekin, S. Kiranyaz, M. Gabbouj, Quantum mechanics in computer vision: Automatic object extraction, in: Proc. IEEE Int. Conf. Image Process., 2013, pp. 2489–2493. [doi:10.1109/ICIP.2013.6738513](https://doi.org/10.1109/ICIP.2013.6738513).
- [32] A. Youssry, A. El-Rafei, S. Elramly, A quantum mechanics-based framework for image processing and its application to image segmentation, *Quantum Inf. Process.* 14 (10) (2015) 3613–3638. [doi:https://doi.org/10.1007/s11128-015-1072-3](https://doi.org/10.1007/s11128-015-1072-3).
- [33] A. Youssry, A. El-Rafei, R.-G. Zhou, A continuous-variable quantum-inspired algorithm for classical image segmentation, *Quantum Mach. Intell.* 1 (3-4) (2019) 97–111. [doi:https://doi.org/10.1007/s42484-019-00009-2](https://doi.org/10.1007/s42484-019-00009-2).
- [34] Z. Kaisserli, T.-M. Laleg-Kirati, A. Lahmar-Benbernou, A novel algorithm for image representation using discrete spectrum of the schrödinger operator, *Digit. Signal Process.* 40 (2015) 80–87. [doi:https://doi.org/10.1016/j.dsp.2015.01.005](https://doi.org/10.1016/j.dsp.2015.01.005).
- [35] S. Dutta, A. Basarab, B. Georgeot, D. Kouamé, Quantum mechanics-based signal and image representation: Application to denoising, *IEEE Open J. Signal Process.* 2 (2021) 190–206. [doi:10.1109/OJSP.2021.3067507](https://doi.org/10.1109/OJSP.2021.3067507).
- [36] S. Dutta, A. Basarab, B. Georgeot, D. Kouamé, Plug-and-play quantum adaptive denoiser for deconvolving poisson noisy images, *IEEE Access* 9 (2021) 139771–139791. [doi:10.1109/ACCESS.2021.3118608](https://doi.org/10.1109/ACCESS.2021.3118608).

- [37] S. Dutta, A. Basarab, B. Georgeot, D. Kouamé, Poisson image deconvolution by a plug-and-play quantum denoising scheme, in: Proc. 29th Eur. Signal Process. Conf. (EUSIPCO), 2021, pp. 646–650. [doi:10.23919/EUSIPCO54536.2021.9616253](https://doi.org/10.23919/EUSIPCO54536.2021.9616253).
- [38] Y. Eldar, A. Oppenheim, Quantum signal processing, *IEEE Signal Process. Mag.* 19 (6) (2002) 12–32. [doi:10.1109/MSP.2002.1043298](https://doi.org/10.1109/MSP.2002.1043298).
- [39] S. Dutta, N. K. Tuador, J. Michetti, B. Georgeot, D. H. Pham, A. Basarab, D. Kouamé, Quantum denoising-based super-resolution algorithm applied to dental tomography images, in: Proc. IEEE 19th Int. Symp. Biomed. Imag. (ISBI), 2022, pp. 1–4. [doi:10.1109/ISBI52829.2022.9761623](https://doi.org/10.1109/ISBI52829.2022.9761623).
- [40] S. Dutta, A. Basarab, B. Georgeot, D. Kouamé, Image denoising inspired by quantum many-body physics, in: Proc. 28th IEEE Int. Conf. Image Process. (ICIP), 2021, pp. 1619–1623. [doi:10.1109/ICIP42928.2021.9506794](https://doi.org/10.1109/ICIP42928.2021.9506794).
- [41] R. Feynman, R. Leighton, M. Sands, *The Feynman Lectures on Physics*, Addison-Wesley world student series, Addison-Wesley, 1977. URL NewMillenniumed.NewYork,NY,USA.2010.
- [42] L. Landau, E. Lifshitz, *Quantum Mechanics: Non-Relativistic Theory*, Course of theoretical physics, Elsevier Science, 1991. URL <https://books.google.fr/books?id=J9ui6KwC4mMC>
- [43] C. Cohen-Tannoudji, B. Diu, F. Laloë, *Quantum Mechanics*, 1st ed, New York, NY, USA: Wiley, 1977. URL https://books.google.fr/books?id=tVL_EAAAQBAJ
- [44] P. Anderson, *Absence of diffusion in certain random lattices*, *Phys. Rev.* 109 (1958) 1492–1505. [doi:10.1103/PhysRev.109.1492](https://doi.org/10.1103/PhysRev.109.1492). URL <https://link.aps.org/doi/10.1103/PhysRev.109.1492>
- [45] G. Mahan, K. Subbaswamy, *Local Density Theory of Polarizability*, Physics of Solids and Liquids, Springer US, 2013. URL <https://books.google.fr/books?id=7v0ICAAQBAJ>
- [46] J. Salmon, Z. Harmany, C.-A. Deledalle, R. Willett, Poisson noise reduction with non-local pca, *J. math. imag. vis.* 48 (2) (2014) 279–294. [doi:https://doi.org/10.1007/s10851-013-0435-6](https://doi.org/10.1007/s10851-013-0435-6).
- [47] M. Makitalo, A. Foi, Optimal inversion of the anscombe transformation in low-count poisson image denoising, *IEEE Trans. Image Process.* 20 (1) (2011) 99–109. [doi:10.1109/TIP.2010.2056693](https://doi.org/10.1109/TIP.2010.2056693).
- [48] S. Liu, L. Gao, Y. Lei, M. Wang, Q. Hu, X. Ma, Y. Zhang, Sar speckle removal using hybrid frequency modulations, *IEEE Trans. Geosci. Remote Sens.* 59 (5) (2021) 3956–3966. [doi:10.1109/TGRS.2020.3014130](https://doi.org/10.1109/TGRS.2020.3014130).
- [49] Y. Yu, S. Acton, Speckle reducing anisotropic diffusion, *IEEE Trans. Image Process.* 11 (11) (2002) 1260–1270. [doi:10.1109/TIP.2002.804276](https://doi.org/10.1109/TIP.2002.804276).
- [50] C. Santos, D. Martins, N. Mascarenhas, Ultrasound image despeckling using stochastic distance-based bm3d, *IEEE Trans. Image Process.* 26 (6) (2017) 2632–2643. [doi:10.1109/TIP.2017.2685339](https://doi.org/10.1109/TIP.2017.2685339).
- [51] A. Achim, A. Bezerianos, P. Tsakalides, Novel bayesian multiscale method for speckle removal in medical ultrasound images, *IEEE Trans. Med. Imag.* 20 (8) (2001) 772–783. [doi:10.1109/42.938245](https://doi.org/10.1109/42.938245).
- [52] J.-S. Lee, Digital image enhancement and noise filtering by use of local statistics, *IEEE Trans. Pattern Anal. Mach. Intell. PAMI-2* (2) (1980) 165–168. [doi:10.1109/TPAMI.1980.4766994](https://doi.org/10.1109/TPAMI.1980.4766994).
- [53] S. Dutta, A. Basarab, B. Georgeot, D. Kouamé, Despeckling ultrasound images using quantum many-body physics, in: Proc. IEEE Int. Ultrason. Symp. (IUS), 2021, pp. 1–4. [doi:10.1109/IUS52206.2021.9593778](https://doi.org/10.1109/IUS52206.2021.9593778).
- [54] Y. Chen, T. Pock, Trainable nonlinear reaction diffusion: A flexible framework for fast and effective image restoration, *IEEE Trans. Pattern Anal. Mach. Intell.* 39 (6) (2017) 1256–1272. [doi:10.1109/TPAMI.2016.2596743](https://doi.org/10.1109/TPAMI.2016.2596743).
- [55] K. Zhang, W. Zuo, L. Zhang, Ffdnet: Toward a fast and flexible solution for cnn-based image denoising, *IEEE Trans. Image Process.* 27 (9) (2018) 4608–4622. [doi:10.1109/TIP.2018.2839891](https://doi.org/10.1109/TIP.2018.2839891).
- [56] K. Zhang, W. Zuo, Y. Chen, D. Meng, L. Zhang, Beyond a gaussian denoiser: Residual learning of deep cnn for image denoising, *IEEE Trans. Image Process.* 26 (7) (2017) 3142–3155. [doi:10.1109/TIP.2017.2662206](https://doi.org/10.1109/TIP.2017.2662206).

SUPPLEMENTARY MATERIAL:

FOR

A NOVEL IMAGE DENOISING ALGORITHM USING CONCEPTS OF QUANTUM MANY-BODY THEORY

Sayantan Dutta^{1,2}, Adrian Basarab³, Bertrand Georgeot², and Denis Kouamé¹

¹Institut de Recherche en Informatique de Toulouse, UMR CNRS 5505, Université de Toulouse, France

²Laboratoire de Physique Théorique, Université de Toulouse, CNRS, UPS, France

³Université de Lyon, INSA-Lyon, Université Claude Bernard Lyon 1, UJM-Saint Etienne, CNRS, Inserm, CREATIS UMR 5220, U1206, Villeurbanne, France.

In this paper, a novel image restoration and denoising algorithm inspired by the quantum many-body theory has been discussed, precisely, using interactions between image patches. To illustrate the interest of the proposed approach in image denoising problems and explore ways to choose the suitable hyperparameters, we study in this supplementary file the optimal hyperparameter values for four different levels of noise intensities with image independent (Gaussian) and dependent (Poisson) noise models. We also present additional information on comparisons of our procedure to other contemporary methods, as well as on a real-life medical application on ultrasound image despeckling.

A. Proposed De-QuIP algorithm

The complete denoising process is summarized in the following Algorithm 1.

Algorithm 1: De-QuIP algorithm

Input: \mathbf{y} , P_h , W_h , d , p , $\hbar^2/2m$

1 Divide the noisy image \mathbf{y} into small patches of size P_h ; say total number is T_{patch} . So, the patch dimension $P_{dim} = P_h^2$

2 **for** $w = 1 : T_{patch}$ **do**

3 Choose one small image patch \mathbf{J}_w

4 Create a search window of size W_h centering at \mathbf{J}_w and using cyclic boundary conditions

5 Collect all the small image patches inside this search window; say the total number is S_{patch}

6 **for** $l = 1 : S_{patch}$ **do**

7 Calculate Euclidean distance D_{wl} between the \mathbf{J}_w and \mathbf{J}_l patch inside the search window

8 Calculate interaction \mathbf{I}_{wl} between the \mathbf{J}_w and \mathbf{J}_l patch inside the search window as,

9
$$\mathbf{I}_{wl}^k = p \frac{|\mathbf{J}_w^k - \mathbf{J}_l^k|}{D_{wl}^2}, \quad k = 1, \dots, P_{dim}$$

10 Calculate total interaction \mathbf{I}_w^{total} between the patch \mathbf{J}_w and the patches inside the search window by taking sum over all l ; i.e.,

11
$$\mathbf{I}_w^{total} = \sum_{l=1}^{S_{patch}} \mathbf{I}_{wl}^k, \quad k = 1, \dots, P_{dim}$$

12 Effective potential for the \mathbf{J}_w patch is $\mathbf{V}_w^{effective} = \mathbf{J}_w^k + \mathbf{I}_w^{total}$, $k = 1, \dots, P_{dim}$

13 Construct the Hamiltonian matrix \mathbf{H}_w using the effective potential $\mathbf{V}_w^{effective}$

14 Calculate the eigenvalues and eigenvectors of \mathbf{H}_w

15 Construct adaptive basis $\mathbf{B}_w^{adaptive}$ using the eigenvectors ψ_w^k , $k = 1, \dots, P_{dim}$

16 Project the noisy patche \mathbf{J}_w onto this adaptive basis $\mathbf{B}_w^{adaptive}$

17 Calculate projection coefficients \mathbf{c}_w in the P_{dim} -dimensional space. Note that, $P_{dim} > d$

18 Redefine the projection coefficients in the d -dim subspace as $\mathbf{c}_w^{new} = \mathbf{c}_w^k, k = 1, \dots, d$

19 Reconstruct the patch by $\mathbf{R}_w = \sum_{k=1}^d \mathbf{c}_w^{new} \psi_w^k$

20 Combining all T_{patch} number of small denoised image patches \mathbf{R}_w restores the full denoised image $\hat{\mathbf{x}}$

Output: $\hat{\mathbf{x}}$

B. Computational complexity

In the precedingly developed algorithm based on single particle quantum physics [35], the computational complexity of the algorithm was essentially controlled by the diagonalization of a large Hamiltonian matrix and the identification of its eigenvectors. For an image of size $n \times n$, this matrix is $n^2 \times n^2$. In general, for an arbitrary matrix, the diagonalization process would require $O(n^6)$ operations and $O(n^4)$ storage space. However, for a highly sparse matrix (like the Hamiltonian matrix), efficient iterative methods such as the Lanczos method reduce the computational complexity to $O(n^4)$ operations with $O(n^4)$ space complexity required for the diagonalization.

In the case of the many patch algorithm, the denoising is done patch-wisely (of size $P_h \times P_h$), the time and space complexity become $O(P_h^4)$ for each denoise region, much smaller than the previous one for $P_h \ll n$. Yet, the best time complexity one can achieve is $O(dP_h^2)$ if one computes only the d eigenvectors used for the restoration task (with $d \leq P_h^2$), with a space complexity also in $O(dP_h^2)$.

The second major contribution comes from the computations of the transform coefficients using an iterative scheme that would require $O(dP_h)$ operations for each denoise region.

The interaction count for each denoise region gives a complexity in total of $O((S_{patch} + 1)P_h)$ if there are S_{patch} patches inside the $W_h \times W_h$ size search window.

Therefore, if the image consists of T_{patch} regions (patches), then the dominant computational cost of the proposed denoising algorithm is $O(T_{patch}dP_h^2)$. Additionally, parallel computation can be used to boost up the process even further.

C. Influence of the proportionality constant p

In Table II, we observed the proportionality constant p values that maximize the output PSNR for the first seven sample images in Fig. 3 (in the primary manuscript) corrupted with four different noise intensities. For the numerical experiment, we consider three different patch sizes when the images are corrupted with image independent (*e.g.*, Gaussian) and dependent (*e.g.*, Poisson) noise models. The observations confirm that there is a tendency for optimal values to decrease as the noise level increases.

TABLE II
OPTIMAL PROPORTIONALITY CONSTANT p FOR DE-QUIP

Sample	Input SNR(dB)	Gaussian case			Poisson case		
		5 × 5	7 × 7	11 × 11	5 × 5	7 × 7	11 × 11
house	22	0.0385	0.0750	0.0550	0.0109	0.0467	0.0800
	16	0.0197	0.0667	0.0700	0.0046	0.0325	0.0900
	8	0.0053	0.0600	0.0625	0.0064	0.0305	0.0500
	2	0.0001	0.0225	0.0475	0.00013	0.0034	0.0400
lake	22	0.0220	0.0900	0.0900	0.0057	0.0555	0.0600
	16	0.0130	0.0522	0.0936	0.0033	0.0269	0.0400
	8	0.0060	0.0460	0.0755	0.0018	0.0355	0.0499
	2	0.0001	0.0290	0.0573	0.00013	0.0096	0.0300
lena	22	0.0215	0.0950	0.1250	0.0156	0.0533	0.0625
	16	0.0107	0.0758	0.1100	0.0067	0.0317	0.0550
	8	0.0046	0.0467	0.0600	0.00031	0.0207	0.0775
	2	0.00001	0.0100	0.0400	0.00001	0.0010	0.0550
hill	22	0.0154	0.0643	0.1229	0.0089	0.0500	0.0900
	16	0.0139	0.0521	0.0888	0.0056	0.0400	0.0800
	8	0.0072	0.0375	0.0625	0.00088	0.0300	0.0629
	2	0.00001	0.0146	0.0340	0.00001	0.0055	0.0429
fingerprint	22	0.0500	0.0700	0.0450	0.0244	0.0600	0.1000
	16	0.0369	0.0657	0.0650	0.0133	0.0400	0.0833
	8	0.0041	0.0543	0.0900	0.00011	0.0350	0.0650
	2	0.0022	0.0110	0.0830	0.00005	0.0011	0.0500
saturn	22	0.0257	0.0700	0.1100	0.0100	0.0500	0.1083
	16	0.0021	0.0578	0.0900	0.0080	0.0400	0.0967
	8	0.0031	0.0234	0.0600	0.0006	0.0124	0.0617
	2	0.00001	0.0157	0.0500	0.00001	0.0010	0.0540
flintstones	22	0.0260	0.0931	0.0463	0.0089	0.0400	0.0500
	16	0.0183	0.0500	0.0304	0.0044	0.0225	0.0655
	8	0.0052	0.0308	0.0500	0.0006	0.0200	0.0525
	2	0.0016	0.0205	0.0500	0.00017	0.0126	0.0450

The linear fit parameters are summarized in Table III together with the ℓ_2 error and the resulting average loss in the denoising performance in terms of PSNR and SSIM. One may notice that the denoising performance loss with rule (9) (in the primary manuscript) rather than the optimal choice is negligible.

D. Influence of the $\hbar^2/2m$ and subspace dimensionality d

The hyperparameter $\hbar^2/2m$ or say F_{factor} controls the frequency distribution across the basis vectors since the maximal frequency of a vector with energy E at the local pixel value V is $\sqrt{(E - V)/(\hbar^2/2m)}$. Hence, the maximal oscillation frequency of the basis vector decreases with increasing F_{factor} . As a consequence, low-energy basis vectors become more prominent to distinguish low and high pixel regions using different levels of frequency. Thus, optimal subspace dimensionality d decreases as F_{factor} grows. These optimal choices vary with the image patch size and noise statistics. Table IV and Table V show these optimal values that give the best output PSNR for the first seven sample images in Fig. 3 (in the primary manuscript) corrupted with image independent (*e.g.*, Gaussian) and dependent (*e.g.*, Poisson) noises with four different noise intensities.

TABLE III

SLOPE AND INTERCEPT USED IN DETERMINING PROPORTIONALITY CONSTANT p FOR VARIOUS PATCH SIZES FOR GAUSSIAN AND POISSON NOISE MODELS. ALSO, THE ASSOCIATIVE ℓ_2 ERROR, PSNR (dB) LOSS AND SSIM LOSS IN LINEAR CURVE FITTING TO THE OPTIMAL p .

		Size of the patches		
		5 × 5	7 × 7	11 × 11
Gaussian	Slope (m_1)	12.84×10^{-4}	30.96×10^{-4}	16.46×10^{-4}
	Intercept (c_1)	-35.96×10^{-4}	13.56×10^{-3}	50.40×10^{-3}
	ℓ_2 error for p fit	0.0327	0.0528	0.1196
	PSNR(dB) loss	0.278	0.306	0.179
	SSIM loss	0.0139	0.0172	0.0106
Poisson	Slope (m_1)	60.33×10^{-5}	21.00×10^{-4}	16.64×10^{-4}
	Intercept (c_1)	-21.85×10^{-4}	36.31×10^{-4}	44.23×10^{-3}
	ℓ_2 error for p fit	0.0189	0.0392	0.0811
	PSNR(dB) loss	0.380	0.422	0.485
	SSIM loss	0.0197	0.0185	0.0150

TABLE IV
OPTIMAL F_{FACTOR} VALUES FOR DE-QUIP

Sample	Input SNR(dB)	Gaussian case			Poisson case		
		5 × 5	7 × 7	11 × 11	5 × 5	7 × 7	11 × 11
house	22	1.4714	2.4250	2.2000	1.7000	2.2667	2.6000
	16	1.9000	1.6733	2.3000	1.6000	1.9167	1.8500
	8	1.9800	1.5333	1.9833	1.9900	2.1000	1.0000
	2	1.5000	1.2000	1.7300	2.9000	1.9000	1.5800
lake	22	1.6000	2.1125	2.4000	1.4889	1.8000	1.6000
	16	1.5500	1.9633	2.8000	1.6333	1.9900	2.0000
	8	2.2000	1.4083	2.0650	2.5000	1.8500	2.0000
	2	1.6632	2.1000	2.3000	2.8333	2.6000	1.7000
lena	22	1.3850	1.9000	2.4000	1.6000	2.0400	2.5000
	16	1.8500	1.7800	2.3000	1.8000	1.8500	2.1000
	8	2.0000	1.5500	2.0200	1.9200	2.2667	1.7000
	2	1.2400	0.8571	2.1000	2.6500	2.2333	2.0000
hill	22	1.3570	1.5000	1.8000	1.6500	1.5182	1.9000
	16	2.4500	2.2500	2.0000	2.0000	2.2000	1.9400
	8	2.6222	2.7400	2.5000	3.0000	3.0000	2.2800
	2	1.6167	2.1444	2.0000	2.5000	2.9000	3.2000
fingerprint	22	1.2500	1.3800	1.4500	1.6000	1.5000	1.5000
	16	1.7000	1.7500	2.1000	1.5400	1.6000	2.3000
	8	3.3000	3.0000	1.8000	3.8000	3.0000	1.9000
	2	2.7000	2.0000	2.0000	3.8000	3.0000	3.6000
saturn	22	1.3500	1.3900	1.9000	1.5500	1.8778	2.2600
	16	1.7818	1.7000	1.7000	1.5600	1.4889	1.8000
	8	1.5909	1.8400	1.8000	2.1143	2.0000	1.9600
	2	1.6286	1.7100	1.7000	1.8333	1.6000	2.0429
flintstones	22	1.4000	1.5500	1.5000	1.8000	1.4000	1.5000
	16	1.9333	1.9000	1.9000	1.7000	1.8400	1.5000
	8	1.8000	2.0000	1.9000	3.0000	1.9700	1.9000
	2	3.0000	2.5750	1.8000	3.8000	2.9000	1.9000

The best-fitted curve parameters to the optimal F_{factor} and d are regrouped in Table VI. These rules give an efficient way to select the hyperparameters close to their optimality with a minimal performance loss depending on the size of the given patch and the intensity of the noise.

TABLE V
OPTIMAL SUBSPACE DIMENSIONALITY d FOR DE-QUIP

Sample	Input SNR(dB)	Gaussian case			Poisson case		
		5 × 5	7 × 7	11 × 11	5 × 5	7 × 7	11 × 11
house	22	16	39	120	15	33	85
	16	10	24	111	10	25	74
	8	6	11	56	3	11	24
	2	3	4	24	2	6	18
lake	22	24	48	84	24	48	120
	16	21	40	64	22	36	101
	8	7	15	25	8	14	36
	2	3	7	11	3	6	24
lena	22	19	35	100	18	33	98
	16	12	21	58	11	22	90
	8	7	8	27	5	8	28
	2	2	4	12	2	4	17
hill	22	25	48	120	24	48	120
	16	20	40	111	22	43	115
	8	6	13	41	6	13	41
	2	3	6	11	2	6	11
fingerprint	22	13	28	86	13	26	86
	16	8	18	56	8	17	47
	8	4	9	28	4	8	18
	2	3	7	19	3	7	13
saturn	22	8	17	51	8	17	47
	16	7	11	30	8	12	30
	8	3	6	15	3	4	15
	2	2	5	7	2	3	7
flintstones	22	24	48	120	24	47	120
	16	13	41	118	14	37	118
	8	8	13	41	8	13	32
	2	5	10	25	4	8	24

TABLE VI

CURVE FITTING PARAMETERS USED IN DETERMINING d AND F_{FACTOR} FOR VARIOUS PATCH SIZES FOR GAUSSIAN AND POISSON NOISE MODELS. ALSO, THE ASSOCIATIVE ℓ_2 ERRORS, PSNR (dB) LOSS AND SSIM LOSS IN CURVE FITTING TO THE OPTIMAL d AND F_{FACTOR} .

		Size of the patches		
		5 × 5	7 × 7	11 × 11
Gaussian	Slope (m_2)	0.7783	1.7000	4.2500
	Intercept (c_2)	0.7315	0.5345	4.8210
	ℓ_2 error for d fit	21.1673	43.3499	112.4127
	Parameter l_1	0.5287	1.2630	1.9161
	Parameter l_2	-4.4551	-4.1915	6.8223
	Parameter l_3	20.6204	13.9698	9.7995
	ℓ_2 error for F_{factor} fit	2.3845	2.6135	1.9334
	PSNR(dB) loss	0.416	0.361	0.209
	SSIM loss	0.0153	0.0129	0.0118
	Slope (m_2)	0.8202	1.6030	4.3990
Poisson	Intercept (c_2)	0.8621	0.5800	2.8900
	ℓ_2 error for d fit	23.2670	43.4135	115.9894
	Parameter l_1	0.8083	1.5391	1.8587
	Parameter l_2	-3.8975	-4.4288	11.6517
	Parameter l_3	16.8476	10.1560	3.9798
	ℓ_2 error for F_{factor} fit	3.3802	2.0652	2.2571
	PSNR(dB) loss	0.487	0.594	0.485
	SSIM loss	0.0175	0.0266	0.0386

E. Denoising efficiency of the proposed scheme in comparison with standard methods

For a comprehensive survey of the denoising ability of De-QuIP, rigorous comparisons with contemporary noise removal methods from the Table VII. Tables VIII and IX compare quantitative performance in terms of PSNR and SSIM in the case of Gaussian and Poisson corrupted images, respectively.

TABLE VII
COMPARISON OF DENOISING PERFORMANCE OF DE-QUIP WITH DIFFERENT PATCH SIZES FOR DIFFERENT NOISE LEVELS.

Sample	Input	Gaussian case						Poisson case						
		5 × 5		7 × 7		11 × 11		5 × 5		7 × 7		11 × 11		
		SNR(dB)	PSNR(dB)	SSIM	PSNR(dB)	SSIM								
house	22	35.30	0.88	35.45	0.89	35.58	0.89	34.94	0.87	35.10	0.88	35.14	0.88	
	16	31.91	0.83	32.15	0.83	32.29	0.83	31.49	0.82	31.78	0.82	31.73	0.82	
	8	26.85	0.72	27.45	0.75	27.91	0.76	26.45	0.72	27.02	0.74	27.27	0.75	
	2	23.05	0.60	23.92	0.68	24.66	0.72	22.65	0.59	23.48	0.66	24.09	0.70	
lake	22	33.23	0.92	33.16	0.91	32.80	0.90	33.09	0.91	33.04	0.90	32.72	0.90	
	16	28.81	0.83	28.85	0.82	28.63	0.81	28.54	0.81	28.60	0.81	28.42	0.81	
	8	24.05	0.69	24.19	0.71	24.37	0.69	23.75	0.66	23.98	0.68	24.11	0.68	
	2	21.09	0.57	21.59	0.62	21.75	0.63	20.90	0.56	21.33	0.61	21.48	0.63	
lena	22	35.05	0.89	35.21	0.89	35.34	0.90	34.86	0.88	35.05	0.89	35.16	0.89	
	16	31.73	0.84	32.00	0.85	32.17	0.85	31.49	0.83	31.78	0.84	32.34	0.84	
	8	26.17	0.71	27.67	0.78	28.00	0.78	26.93	0.74	27.40	0.77	27.61	0.76	
	2	23.60	0.63	24.53	0.71	25.04	0.74	23.36	0.63	24.30	0.71	24.71	0.71	
hill	22	31.54	0.82	31.58	0.83	31.55	0.83	32.01	0.82	32.16	0.83	32.13	0.83	
	16	27.95	0.69	28.06	0.70	28.10	0.70	28.25	0.70	28.37	0.70	28.39	0.70	
	8	24.42	0.55	24.49	0.55	24.61	0.55	24.58	0.55	24.63	0.55	23.58	0.54	
	2	21.97	0.46	22.41	0.48	22.61	0.49	22.08	0.46	22.46	0.48	22.54	0.49	
fingerprint	22	32.35	0.93	32.50	0.93	32.54	0.94	33.39	0.94	32.15	0.93	33.49	0.95	
	16	28.12	0.86	28.46	0.87	28.65	0.87	28.63	0.87	28.16	0.86	28.24	0.86	
	8	23.36	0.72	23.31	0.72	23.63	0.73	23.65	0.74	23.07	0.72	23.40	0.73	
	2	20.03	0.59	19.80	0.57	20.01	0.58	19.90	0.59	19.58	0.56	19.56	0.56	
saturn	22	38.94	0.89	39.36	0.92	39.53	0.94	40.64	0.97	40.85	0.98	40.87	0.98	
	16	34.67	0.79	35.27	0.83	35.63	0.87	36.00	0.94	36.31	0.95	36.42	0.94	
	8	28.94	0.61	29.87	0.67	30.60	0.74	30.44	0.89	31.00	0.90	31.40	0.89	
	2	24.45	0.46	25.97	0.55	27.03	0.62	26.40	0.82	27.26	0.86	27.46	0.85	
flintstones	22	32.20	0.87	32.16	0.87	31.97	0.86	33.20	0.88	33.08	0.88	32.99	0.88	
	16	28.65	0.80	28.69	0.79	28.47	0.78	29.04	0.80	29.00	0.78	28.77	0.78	
	8	23.48	0.67	23.78	0.68	23.70	0.66	23.44	0.65	23.84	0.68	23.64	0.64	
	2	19.74	0.52	19.87	0.56	20.03	0.56	19.50	0.51	19.69	0.53	19.63	0.53	

F. Application to ultrasound (US) image despeckling

The despeckling performance of De-QuIP is investigated through a phantom as well as four real cancer and two non-cancer thyroid US images acquired with a 7.5 MHz linear probe. For the quantitative analysis, the contrast-to-noise-ratio (CNR) and resolution loss (RL) are regrouped in Table X and in Fig. 14 for a visual demonstrations. Observation shows that De-QuIP offers a better image contrast (higher CNR than AD, Lee and slightly lower than NLM, which over-smooths the images and yields poor resolution) while having less spatial resolution loss (De-QuIP has less spatial resolution loss compared to the native US image). Note that these images are chosen arbitrarily, that is, the quality of the results should not depend on the data tested.

TABLE VIII

QUANTITATIVE DENOISING RESULTS FOR GAUSSIAN CORRUPTED IMAGES (AVERAGE OVER 10 INDEPENDENT NOISE REALIZATIONS). THE BEST VALUES ARE HIGHLIGHTED BY COLOR.

Sample	Input SNR	Methods													
		PND		PGPCA		PLPCA		BM3D		DL		GSP		QAB	
		PSNR	SSIM	PSNR	SSIM	PSNR	SSIM	PSNR	SSIM	PSNR	SSIM	PSNR	SSIM	PSNR	SSIM
house	22	33.17	0.831	34.28	0.863	34.80	0.866	35.89	0.896	32.86	0.827	35.70	0.891	33.77	0.856
	16	30.78	0.800	31.13	0.803	31.47	0.802	33.05	0.848	29.72	0.747	32.91	0.839	30.16	0.767
	8	27.52	0.753	26.83	0.672	26.65	0.605	28.73	0.786	25.31	0.587	28.19	0.760	25.71	0.601
	2	24.25	0.679	23.45	0.491	22.63	0.371	24.96	0.706	21.20	0.405	23.93	0.589	22.92	0.464
lake	22	30.29	0.855	32.36	0.895	32.56	0.895	33.07	0.919	30.90	0.863	32.09	0.913	32.22	0.878
	16	26.78	0.780	28.21	0.815	28.39	0.814	28.92	0.857	27.22	0.768	28.45	0.836	28.59	0.795
	8	23.61	0.697	23.87	0.653	23.77	0.606	24.43	0.739	23.25	0.588	24.30	0.722	24.24	0.599
	2	21.42	0.623	21.23	0.483	20.73	0.388	21.97	0.652	20.16	0.419	21.27	0.548	20.79	0.441
lena	22	33.52	0.858	34.78	0.881	35.04	0.883	35.50	0.898	34.08	0.868	35.09	0.893	34.36	0.876
	16	31.10	0.822	31.75	0.831	31.95	0.829	32.70	0.861	30.93	0.801	32.43	0.852	31.02	0.801
	8	27.94	0.773	27.65	0.716	27.35	0.648	28.75	0.799	26.34	0.638	28.18	0.767	26.61	0.657
	2	25.21	0.716	24.27	0.536	23.34	0.415	25.57	0.728	22.27	0.446	24.93	0.664	22.76	0.476
hill	22	29.35	0.742	30.98	0.812	31.29	0.819	31.36	0.818	29.80	0.761	30.97	0.811	30.56	0.810
	16	26.90	0.640	27.86	0.690	28.07	0.700	28.32	0.710	27.17	0.649	28.15	0.708	27.24	0.671
	8	24.34	0.534	24.55	0.539	24.42	0.515	24.98	0.575	23.85	0.478	24.86	0.571	23.91	0.492
	2	22.49	0.475	22.24	0.405	21.75	0.345	22.72	0.493	21.14	0.354	22.33	0.447	21.39	0.375
fingerprint	22	28.40	0.845	31.14	0.912	31.30	0.914	31.47	0.917	29.79	0.882	31.23	0.896	30.32	0.894
	16	25.57	0.757	27.27	0.830	27.46	0.835	27.92	0.850	25.97	0.783	26.99	0.824	27.16	0.815
	8	22.58	0.666	22.73	0.680	23.02	0.676	23.77	0.734	21.09	0.575	23.22	0.698	22.95	0.671
	2	20.05	0.563	18.92	0.471	19.50	0.474	20.73	0.613	17.85	0.385	20.21	0.546	20.04	0.527
saturn	22	40.95	0.955	39.32	0.935	39.63	0.929	42.26	0.970	37.55	0.891	41.20	0.943	38.63	0.916
	16	37.86	0.904	35.80	0.907	36.02	0.883	38.64	0.937	33.74	0.776	38.01	0.881	34.44	0.850
	8	32.23	0.775	30.70	0.753	30.09	0.647	33.16	0.861	28.00	0.541	32.58	0.757	29.44	0.712
	2	28.13	0.640	26.68	0.544	25.31	0.398	28.31	0.747	23.36	0.347	27.64	0.608	25.27	0.601
flintstones	22	28.54	0.766	30.62	0.827	30.83	0.831	31.31	0.847	29.15	0.793	30.91	0.841	30.34	0.811
	16	25.63	0.702	27.36	0.755	27.61	0.758	28.61	0.802	25.64	0.695	28.33	0.776	27.68	0.752
	8	21.86	0.620	22.15	0.586	22.31	0.567	23.96	0.705	21.12	0.520	23.61	0.662	22.54	0.561
	2	18.79	0.521	18.67	0.415	18.62	0.364	20.12	0.585	17.86	0.361	19.38	0.498	19.17	0.435
ridges	22	46.41	0.985	47.52	0.980	47.18	0.973	50.58	0.993	44.49	0.968	47.76	0.980	46.47	0.956
	16	42.32	0.961	43.34	0.950	42.97	0.938	45.37	0.978	40.17	0.922	42.60	0.931	41.44	0.898
	8	32.65	0.816	38.03	0.856	37.09	0.828	38.60	0.922	33.60	0.779	37.06	0.859	34.68	0.754
	2	25.99	0.599	33.07	0.720	31.91	0.672	33.56	0.837	28.97	0.618	33.15	0.727	29.86	0.643
peppers	22	31.23	0.842	32.83	0.871	33.06	0.872	33.79	0.897	31.32	0.840	33.34	0.891	32.08	0.849
	16	28.46	0.801	29.39	0.814	29.70	0.811	30.58	0.853	28.02	0.762	30.25	0.839	28.67	0.758
	8	24.54	0.744	24.93	0.674	25.03	0.639	26.24	0.771	23.96	0.608	26.07	0.752	23.94	0.612
	2	21.73	0.687	21.67	0.519	21.38	0.420	22.83	0.683	20.43	0.434	21.96	0.579	20.49	0.457
bridge	22	27.91	0.751	29.90	0.839	30.08	0.845	30.11	0.846	28.72	0.799	29.43	0.824	29.27	0.817
	16	25.16	0.608	26.28	0.685	26.46	0.697	26.57	0.698	25.52	0.655	26.33	0.693	25.78	0.662
	8	22.53	0.464	22.82	0.499	22.82	0.493	23.12	0.511	22.27	0.467	23.00	0.508	22.31	0.472
	2	20.69	0.393	20.61	0.372	20.29	0.337	21.00	0.421	19.71	0.333	20.60	0.389	20.04	0.362
cameraman	22	30.25	0.812	32.66	0.880	32.97	0.881	33.54	0.907	31.54	0.858	32.71	0.882	32.13	0.865
	16	27.29	0.757	28.78	0.793	29.08	0.792	29.99	0.843	27.98	0.758	29.17	0.840	28.18	0.751
	8	24.28	0.695	24.42	0.635	24.45	0.579	25.80	0.755	23.72	0.581	25.54	0.751	23.93	0.612
	2	21.78	0.617	21.45	0.434	21.03	0.347	22.77	0.674	20.28	0.393	22.13	0.597	20.51	0.402

- PND → Principal Neighborhood Dictionaries [16]
- PGPCA → Patch-based Global Principal Component Analysis [17]
- PLPCA → Patch-based Local Principal Component Analysis [17]
- BM3D → Block-Matching and 3D Filtering [13]
- DL → Dictionary Learning [12]
- GSP → Graph Signal Processing [6]
- QAB → Quantum Adaptive Basis [35]
- De-QuIP → Denoising by Quantum Interactive Patches (proposed)

TABLE IX

QUANTITATIVE DENOISING RESULTS FOR POISSON CORRUPTED IMAGES (AVERAGE OVER 10 INDEPENDENT NOISE REALIZATIONS). THE BEST VALUES ARE HIGHLIGHTED BY COLOR.

Sample	Input	Methods									
		PNLPCA		ATBM3D		QAB		De-QuIP			
SNR	PSNR	SSIM	PSNR	SSIM	PSNR	SSIM	PSNR	SSIM	PSNR	SSIM	
house	22	33.19	0.848	35.36	0.879	32.85	0.833	35.27	0.879		
	16	30.64	0.815	33.13	0.851	29.18	0.738	32.79	0.839		
	8	26.72	0.706	28.48	0.731	25.63	0.619	27.72	0.757		
	2	20.93	0.519	23.96	0.549	21.02	0.413	23.94	0.651		
lake	22	30.23	0.884	32.13	0.913	31.21	0.845	32.43	0.892		
	16	27.45	0.832	28.69	0.854	27.76	0.789	28.62	0.839		
	8	22.42	0.675	24.50	0.698	23.29	0.567	24.28	0.707		
	2	19.38	0.494	21.65	0.534	20.70	0.418	21.51	0.637		
lena	22	32.68	0.852	34.92	0.886	34.29	0.872	35.15	0.889		
	16	30.74	0.846	32.39	0.856	30.65	0.791	31.87	0.827		
	8	26.19	0.686	28.08	0.751	25.83	0.617	27.78	0.768		
	2	21.76	0.541	24.23	0.599	21.88	0.436	24.63	0.707		
hill	22	30.88	0.792	31.81	0.813	30.89	0.824	31.69	0.824		
	16	26.24	0.673	28.14	0.696	27.44	0.682	27.89	0.696		
	8	22.95	0.535	24.98	0.555	24.45	0.494	24.71	0.548		
	2	19.59	0.413	22.37	0.445	21.80	0.397	22.48	0.480		
fingerprint	22	27.95	0.846	31.40	0.913	30.74	0.905	32.39	0.924		
	16	26.81	0.820	28.41	0.860	27.62	0.829	28.36	0.862		
	8	21.94	0.686	23.63	0.719	22.91	0.679	23.56	0.732		
	2	19.42	0.538	20.16	0.569	20.07	0.549	20.01	0.565		
saturn	22	39.36	0.942	41.15	0.976	38.94	0.906	40.96	0.978		
	16	35.85	0.909	37.39	0.957	34.42	0.849	36.71	0.942		
	8	28.55	0.851	30.82	0.874	28.75	0.714	30.31	0.890		
	2	24.87	0.740	26.20	0.765	24.58	0.591	27.12	0.845		
flintstones	22	30.08	0.820	31.72	0.843	30.29	0.789	32.28	0.864		
	16	28.12	0.796	29.46	0.814	27.23	0.678	29.31	0.806		
	8	22.51	0.631	23.93	0.650	23.67	0.529	23.76	0.668		
	2	18.23	0.435	19.97	0.479	21.08	0.389	19.72	0.532		
ridges	22	42.67	0.942	48.98	0.991	45.59	0.947	47.93	0.986		
	16	39.95	0.894	43.88	0.988	42.23	0.902	42.97	0.965		
	8	31.92	0.630	38.33	0.898	34.64	0.734	37.09	0.865		
	2	26.42	0.491	33.00	0.815	29.83	0.602	31.79	0.816		
peppers	22	31.85	0.860	33.35	0.893	31.42	0.816	33.32	0.889		
	16	30.02	0.847	30.49	0.855	27.78	0.737	29.97	0.830		
	8	25.08	0.693	25.97	0.743	23.02	0.587	25.45	0.737		
	2	20.61	0.532	22.19	0.591	19.74	0.434	21.69	0.676		
bridge	22	28.59	0.734	29.22	0.800	30.49	0.847	30.58	0.860		
	16	25.99	0.660	26.61	0.690	26.44	0.689	26.50	0.694		
	8	22.37	0.471	23.16	0.512	23.13	0.472	22.65	0.496		
	2	19.46	0.351	20.94	0.413	20.17	0.352	20.56	0.398		
cameraman	22	29.48	0.855	32.45	0.881	31.77	0.837	32.41	0.890		
	16	28.03	0.821	29.86	0.839	27.78	0.720	28.76	0.818		
	8	23.87	0.645	25.83	0.734	23.12	0.524	24.87	0.716		
	2	19.39	0.470	22.37	0.546	19.41	0.359	22.08	0.612		

PNLPCA → Poisson Non-Local Principal Component Analysis [46]
QAB → Quantum Adaptive Basis [35]

ATBM3D → Anscombe Transform with Block-Matching and 3D Filtering [47]
De-QuIP → Denoising by Quantum Interactive Patches (proposed)

TABLE X

QUANTITATIVE DESPECKLING RESULTS OF REAL MEDICAL US IMAGES USING DIFFERENT METHODS. THE BEST VALUES ARE HIGHLIGHTED BY COLOR.

Sample	Input	Methods									
		AD		Lee		NLM		De-QuIP			
CNR	CNR	RL (%)	CNR	RL (%)	CNR	RL (%)	CNR	RL (%)	CNR	RL (%)	
phantom	0.69	7.97	6.9	12.25	7.0	15.92	7.2	14.29	7.0		
non-cancer 1	9.56	15.39	7.0	18.04	7.6	19.97	8.5	18.54	7.8		
non-cancer 2	1.86	7.05	6.0	9.77	6.7	11.89	8.4	10.54	7.3		
cancer 1	1.41	4.59	7.5	5.41	8.0	8.43	8.8	9.10	8.1		
cancer 2	0.49	6.14	6.8	8.91	7.9	11.80	9.0	9.92	7.6		
cancer 3	0.96	4.12	6.9	6.12	8.4	8.20	9.4	6.40	8.5		
cancer 4	1.22	5.35	7.3	6.90	9.2	9.04	11.6	7.24	9.6		

AD → Anisotropic Diffusion [49]
Lee → Lee Filtering [52]
NLM → Non-Local Means [16]
De-QuIP → Denoising by Quantum Interactive Patches (proposed)

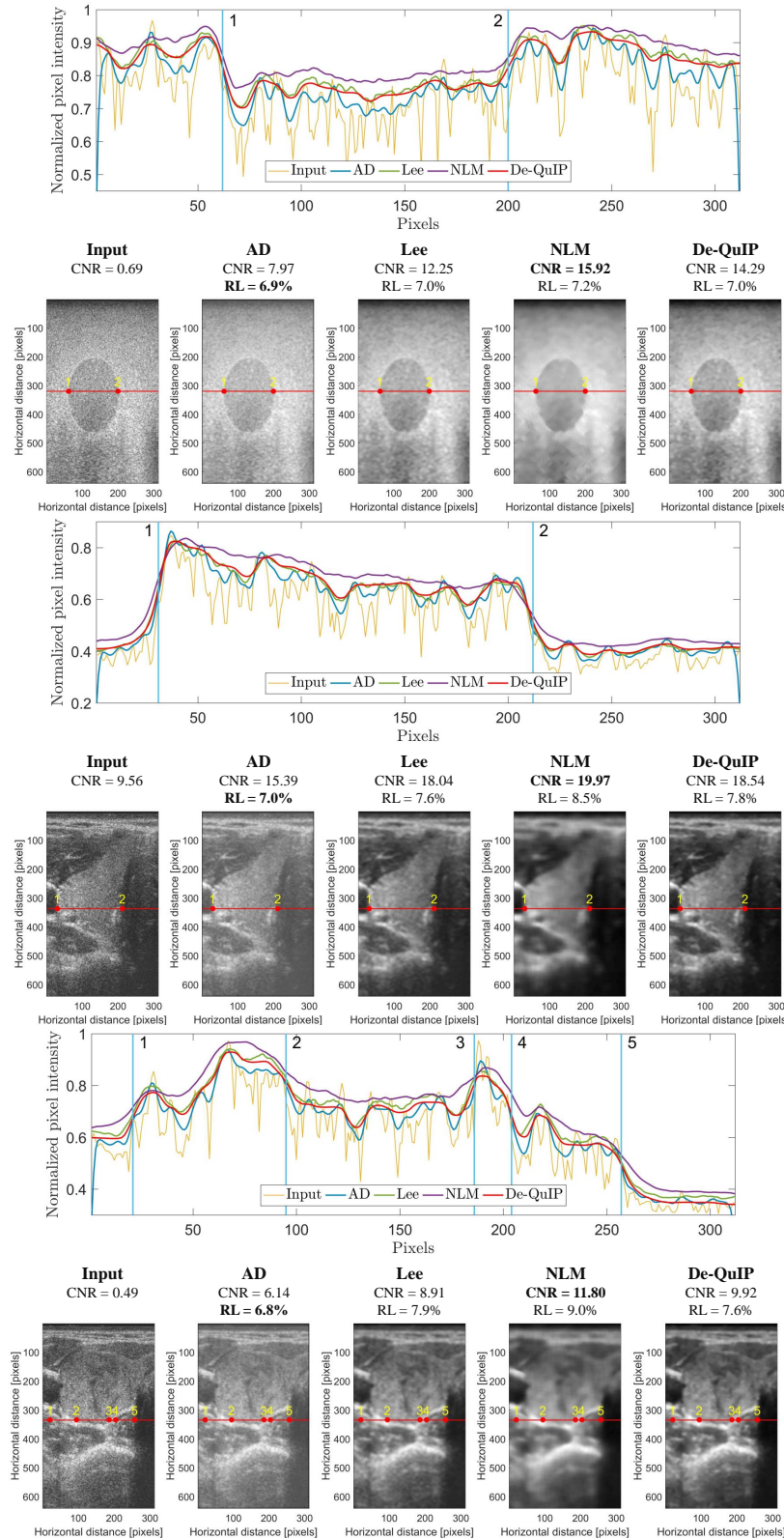


Fig. 14. US image despeckling results using different methods. The top one is the phantom image, the second one is the non-cancer image, and the bottom one is associated with cancer images. The normalized pixel intensities of the extracted red lines from speckled and despeckled US images are shown.